CHALMERS
UNIVERSITY OF TECHNOLOGY

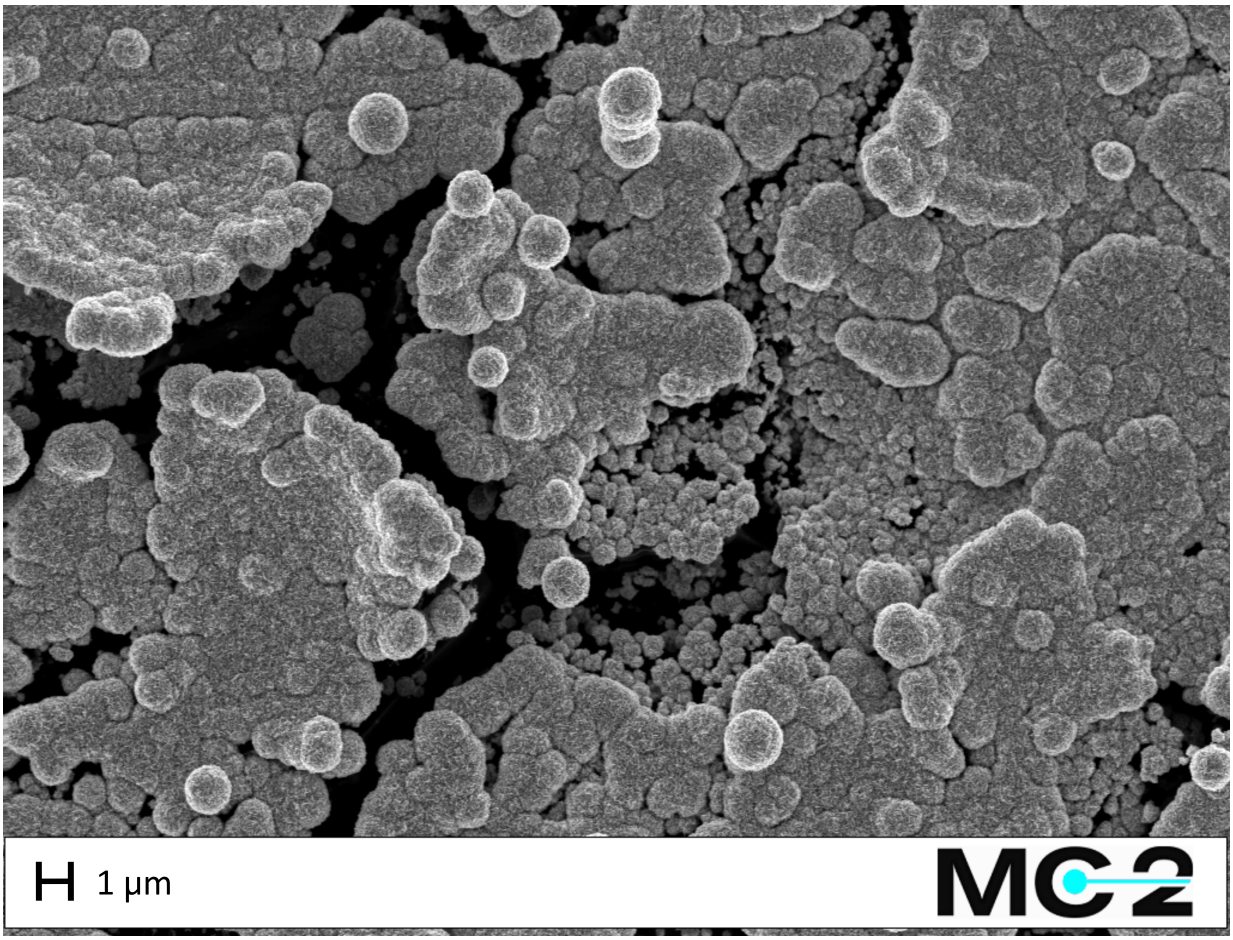

Electrochemical investigations of Pt–Hg and Cu–Hg alloys for mercury decontamination purposes

Master's thesis in Physics

JULIA JÄRLEBARK

Department of Physics
CHALMERS UNIVERSITY OF TECHNOLOGY
Gothenburg, Sweden 2021

Master's thesis 2021: NN

Electrochemical investigations of Pt–Hg and Cu–Hg alloys for mercury decontamination purposes

JULIA JÄRLEBARK

CHALMERS
UNIVERSITY OF TECHNOLOGY

Department of Physics
Division of Chemical Physics
Electrochemistry group
Chalmers University of Technology
Gothenburg, Sweden 2021

Electrochemical investigations of Pt−Hg and Cu−Hg alloys for mercury decontamination purposes
Julia Järlebark

Supervisor: Björn Wickman, Department of Physics
Examiner: Björn Wickman, Department of Physics

Master's Thesis 2021: NN
Department of Physics
Division of Chemical Physics
Electrochemistry group
Chalmers University of Technology
SE-412 96 Gothenburg
Telephone +46 31 772 1000

Cover: SEM image of a platinum black surface.

Typeset in LaTeX
Printed by Chalmers Reproservice
Gothenburg, Sweden 2021

Electrochemical investigations of Pt−Hg and Cu−Hg alloys for mercury decontamination purposes

JULIA JÄRLEBARK
Department of Physics
Chalmers University of Technology

Abstract

Mercury is a heavy metal of large environmental concern due to its potential to spread and bioaccumulate and to its high toxicity for all living organisms. To date, there is no method capable of efficient and sustainable removal of mercury from aqueous solutions under a wide range of conditions. The focus of this thesis is to investigate several aspects of mercury removal by electrochemical alloy formation between mercury and platinum or copper. Mercury ions in the solution are reduced by the application of an electric potential, and form an alloy with a solid platinum or copper electrode. Using an electrochemical quartz crystal microbalance, the temperature dependence of the alloy formation between mercury and platinum is studied in the range $20 - 60$ °C, and the apparent activation energy of the reaction is determined to be 0.29 eV. Another purpose of the thesis is to relate the structure of the electrode at various length-scales to the rate of mercury removal. The electrochemical surface area is determined by underpotential deposition of hydrogen and by measurements of the electrical double-layer capacitance, and the electrode structure is studied using a scanning electron microscope. Mercury removal rates are determined through batch experiments with subsequent inductively coupled plasma mass spectrometry analysis. It can be concluded that a surface area with feature size of the order of 1 mm, e.g. a metal foam, generates an enhanced rate of mercury removal. On the other hand, a nanoporous material with feature size of the order of 100 nm, such as platinum black, does not contribute to an increased mercury removal rate. Two case studies investigating the applicability of the technology are also performed within the thesis; removal of mercury from concentrated sulphuric acid produced by Boliden in the commercial smelting plant in Kokkola and from scrubber liquids from a combined heat and power plant. Mercury is successfully removed from the scrubber liquids using platinum coated titanium fibre electrodes, and from the sulphuric acid using platinum coated stainless steel electrodes. In the case of the sulphuric acid, it is also demonstrated that the process can be scaled up 400 times without loss of efficiency.

Keywords: mercury, heavy metal, electrochemistry, alloy, decontamination, water treatment.

Acknowledgements

First, I would like to express my sincere gratitude to my supervisor, examiner and mentor Björn Wickman, for giving me the opportunity to work on this research project for the last 2.5 years and for his invaluable advice, support and feedback throughout this time. I am also very grateful to Stellan Holgersson and Vera Roth for taking their time to perform the ICP-MS analysis, and to Rosemary Brown for kindly assisting with the electrode fabrication. I would also like to thank all members of the electrochemistry group and the division of Chemical Physics for contributing to an open and welcoming research environment, and for everything I have learned from all our scientific discussions. A special thanks goes to Johan Björkquist, Emma Hanaeus and Alexander Arnens at Atium for all their support, and for the opportunity to work on the applications and case studies in this project. Finally, I want to thank my family and friends for always encouraging me and believing in me; this thesis would not have been possible without them.

Julia Järlebark, Gothenburg, April 2021

Contents

List of Figures

List of Tables

List of Abbreviations

Abbreviation	Meaning
CE	Counter electrode
CV	Cyclic voltammetry
ECSA	Electrochemical surface area
EQCM	Electrochemical quartz crystal microbalance
ICP-MS	Inductively coupled plasma mass spectrometry
ICP-OES	Inductively coupled plasma optical emission spectroscopy
LSV	Linear sweep voltammetry
PVD	Physical vapour deposition
RE	Reference electrode
RF	Roughness factor
SEM	Scanning electron microscopy
SHE	Standard hydrogen electrode
SS	Stainless steel
WE	Working electrode

1

Introduction

Mercury contamination is one of the major environmental issues of the present and the future. Estimates show that mercury exposure poses a threat to the health of 8−10 million people [1, 2]. Mercury is a highly mobile and toxic heavy metal, which since many years has been, and still is, emitted to the atmosphere by anthropogenic processes. Once emitted to the environment, mercury cycles between the atmosphere, land and oceans and can affect the environment for up to 10 000 years [3]. Therefore, being able to remove mercury from both natural waters and industrial wastewaters is of great importance. The mercury decontamination methods available today often have inherent limitations when it comes to mercury concentration, pH, selectivity, or environmental or economical sustainability. Recently, a new technique for mercury decontamination based on electrochemical alloy formation between mercury and platinum or mercury and copper was presented [4, 5]. A negative potential is applied to a platinum or copper electrode, which reduces mercury ions from the solution and allow them to form an alloy with the electrode material. This method provides several advantages compared to current decontamination techniques and is the topic for this thesis.

1.1 Aim of the project

The aim of this thesis has been to further investigate the electrochemical alloy formation between mercury and platinum, and mercury and copper. The purpose of these investigations has been to develop a better understanding of the fundamental processes of alloy formation, but also to evaluate the applicability of the alloy formation for practical decontamination in a few different cases. More specifically, the aim of the thesis can be divided into four main parts:

- Investigating the temperature dependence and activation energy of the Pt−Hg alloy formation.
- Relating the electrochemical surface area and structure of the electrode material to the rate of alloy formation for both the Pt−Hg and Cu−Hg systems.
- Evaluating the technique for mercury removal from scrubber liquids from a combined heat and power plant.
- Studying mercury removal from concentrated sulphuric acid by electrochemical alloy formation, and scaling up the process for this specific application.

1.2 Thesis outline

Chapter 2 of this thesis presents a background to the project. Chemical and biogeochemical information about mercury is covered, and the chapter also contains a review of current mercury decontamination techniques as well as the method under investigation in this thesis. In Chapter 3, the theoretical background is established, including electrochemistry, some thermodynamics and the theoretical aspect of the experimental techniques used. In Chapter 4, the electrodes and experimental methods used in the project are described. Chapter 5 presents and discusses the results of the first two parts of the thesis, namely the temperature study and the investigation of surface area in relation to alloy formation rates. Chapter 6 is divided into two case studies, which addresses the issues of mercury removal from scrubber liquids and concentrated sulphuric acid, respectively. Chapter 7 is a conclusion and outlook.

2
Background

The aim of this chapter is to present a background to the current project. In Section 2.1, the toxicity and environmental cycling of mercury are described, and some international guidelines are presented. Section 2.2 consists of a review of current techniques for mercury removal, and in Section 2.3, the method studied in this thesis is introduced: electrochemical alloy formation between mercury and platinum or copper.

2.1 Mercury

Mercury is a toxic heavy metal, which occurs naturally in the Earth's crust, e.g. in the form of cinnabar ore (HgS) [6]. At room temperature, mercury in its elemental form (Hg^0) is a liquid, which can be oxidised to form monovalent inorganic mercury (Hg^+) and divalent inorganic mercury (Hg^{2+}) [7]. Mercury can also be bound to particulate matter in the form of Hg^p, or exist as organic mercury, e.g. methylmercury (MeHg) [3, 7]. Natural processes, such as volcanic activity, releases mercury to the environment, where it cycles between the atmosphere, terrestrial surfaces and waters [3]. Hg^0 has a long life-time in the atmosphere, of the order of 1 year, and hence mercury in this form is mobile and will travel long distances across the Earth in the atmosphere. A consequence of the high mobility of mercury in the atmosphere is that mercury emissions will not only have an impact on a local scale, but also globally. Over time, Hg^0 will be oxidised primarily to Hg^{2+}, which has a much shorter life-time in the atmosphere, ranging from days to weeks. Hg^{2+} deposits to terrestrial and aqueous systems, from which it may again be released to the atmosphere by burning of biomass, or reduction to Hg^0 and subsequent volatilising. The total life-time of mercury in the environment is estimated to $3\ 000 - 10\ 000$ years before it is bound to its final sink; deep-ocean sediments. The natural biogeochemical cycle of mercury is altered by anthropogenic emissions [3]. Sources of anthropogenic mercury emissions include fossil fuel combustion, biomass burning, mining and production of mercury, gold and other metals, cement production, oil refining, dental amalgams and the chlor-alkali industry [3, 6, 8]. Estimates show that anthropogenic emissions amount to $1\ 010 - 4\ 070$ tonnes mercury per year and that the mercury concentration in the atmosphere has increased $300 - 500\%$ due to these emissions [3, 6, 8].

Mercury present in aqueous systems as Hg^{2+} can be converted by methylating microbes to MeHg, the most toxic form of mercury [3]. MeHg is first efficiently bioconcentrated in plankton, after which it has the ability to biomagify in food chains, thus increasing its concentration in predatory animals. It has been shown that the concentration of MeHg can be more than 1 000 000 times higher in marine predators, such as fish, seals and whales, than in the surrounding water [3, 6]. At the current environmental concentrations, MeHg affects the

behaviour, reproduction, hormones and neurochemistry of animals exposed to it, e.g. fish and birds [3]. In humans, exposure to MeHg is known to cause neurological damage, as cognitive dysfunction, numbness, memory loss and disturbances of vision, hearing and sensing [3, 9]. The health effects of mercury exposure also include damage to the brain, heart, lungs, kidney and immune system [2, 9]. Most vulnerable are young children and fetuses, who may suffer from neurological and developmental problems following mercury exposure [3, 9]. One of the main sources for human exposure to mercury is consumption of seafood containing high levels of MeHg [3, 9, 10]. For this reason, women of fertile age are advised not to eat certain species of fish that may contain high levels of mercury more than $2-3$ times per year.

The high toxicity of mercury to both human health and the environment has drawn the attention to this issue, and risen concerns amongst organisations and governments globally. The World Health Organization (WHO) has identified mercury as "one of the top ten chemicals of major public health concern" and the United Nations (UN) considers mercury "a chemical of global concern" [9, 11]. Due to the large impacts of mercury on human health, WHO has set a guideline of 6 μg L^{-1} inorganic mercury for drinking water [12]. The corresponding limit from the European Union (EU) is 1 μg L^{-1} mercury [13]. As large amounts of mercury have already been released to the environment, and still are emitted today, it is evident that mercury decontamination of both natural waters and industrial wastewaters is essential to reduce the impacts of mercury pollution on human health and the environment.

2.2 Mercury removal technologies

There are several factors of great importance to consider when comparing mercury decontamination methods for different applications. The water streams in need of decontamination differ substantially in volume, pH, mercury concentration and chemical composition. A decontamination method should ideally be efficient in a wide variety of conditions and be able to remove mercury below the WHO and EU limits. It must also be cost efficient and have as low negative impact on the environment as possible. Several methods are currently available for mercury decontamination, including precipitation, adsorption, flotation, coagulation and flocculation, membrane filtration, and ion exchange [14–16]. These methods and their inherent strengths and limitations will be described in this section.

2.2.1 Precipitation

Precipitation is the most common method for industrial wastewater treatment [15, 17]. The water is treated by addition of a chemical, e.g. a sulphide salt, which reacts with mercury ions and form insoluble precipitates, e.g. mercury sulphide:

$$Hg^{2+}(aq) + S^{2-}(aq) \leftrightarrows HgS(s) \tag{2.1}$$

Precipitation is often combined with other wastewater treatment methods, such as flocculation and filtration to remove the precipitates. Notable advantages of the precipitation method are its relative simplicity and low price [15, 18]. The precipitation process is however greatly dependent on pH and often requires pre-treatment pH adjustment of the water [17]. In addition, precipitation is not selective for mercury, and will form precipitates with

several other metals in addition to mercury [14]. Selectivity can be an advantage or a disadvantage depending on application. In some cases, it may be advantageous with a wastewater treatment technology that takes care of several different pollutants. However, as other precipitating compounds than mercury are often more abundant, large amounts of chemicals are needed. The consequence of this is generation of large amounts of hazardous mercury-containing sludge, which requires complicated and costly waste management and disposal [14, 15, 17]. Precipitation is effective at high concentrations of mercury, but unable to remove mercury below $10 - 100$ μg L^{-1}, which can be compared with the WHO guideline for safe drinking water at 6 μg L^{-1} [17].

2.2.2 Adsorption

Another effective, relatively simple, and widely used technique for wastewater treatment is adsorption [14, 15, 17, 19]. The most common adsorbent is activated carbon, having a very large surface area of $500 - 1\,500$ m^2 g^{-1} originating from its micro- and mesoporous structure [15, 16, 20]. Aside from its large surface area, the adsorption capacity of activated carbons is often enhanced by the introduction of various functional groups to the surface [20]. Activated carbon is considered an effective adsorbent, in particular for vapour streams, but also for water streams, and can remove mercury at lower concentrations than precipitation [17, 19, 20]. One of the limitations of this technology is the high cost of commercial activated carbon, which has led to investigations of alternative adsorbents [14–16]. In an attempt to make the technology more economically viable, researchers have prepared activated carbon from organic and biological waste, such as eucalyptus bark, peanut hulls and sheep bone [15, 16]. Other low-cost adsorbents that have been suggested are agricultural wastes and biosorbents, including microbes, algae and non-living biomass. The various types of adsorbents all have different mercury removal capacities, and the efficiency is dependent on pH, temperature and saturation of the adsorbent [14, 16]. Typical removal efficiencies reported are in the range of 56 to 99% for initial mercury concentrations of $0.01 - 20$ mg L^{-1}, and typical adsorption capacities are $12 - 227$ mg mercury per gram of adsorbent [16, 17, 19]. Adsorption has low selectivity for mercury, and hence other pollutants will adsorb as well, leading to quicker saturation of the adsorbent. Once saturated, the adsorbents must either be regenerated or processed as hazardous waste [14]. Regeneration is not always possible, and when applicable, is costly and results in loss of adsorbent material [14, 16].

2.2.3 Flotation

Flotation is a method for removing pollutants from water by generating air bubbles, to which the pollutants attach and are brought to the surface [15]. At the water surface, a pollutant-containing sludge is formed and can be separated from the water. There are several different variations of this technology, and especially useful for the removal of heavy metal ions, as mercury, is ion flotation [15, 21]. An amphiphilic surfactant is added to the water, and the ion and surfactant will together attach to the air bubbles, with the hydrophobic group in the air and the hydrophilic in the water. Flotation can be efficient and selective, however both selectivity and efficiency are pH dependent, and both installation and maintenance costs are high [14, 15]. Efficiencies of mercury removal by ion flotation in the range of $99.6 - 99.9$% for an initial mercury concentration of 5 mg L^{-1} have been reported [21].

2.2.4 Coagulation and flocculation

Coagulation is a wastewater treatment technique based on the addition of a coagulant to destabilise colloids[1] in the water, forcing them to form larger aggregates [15]. This is a method generally employed to handle hydrophobic colloids and suspended particles, but can also be useful in reducing the amount of heavy metals in wastewaters. Flocculation is a similar technology, in which a polymer addition to the water helps to aggregate particles. Coagulation and flocculation must be combined with other technologies, e.g. precipitation, flotation and filtration, for efficient removal of heavy metals. Advantages of these methods for mercury removal are the simplicity and the low cost, and disadvantages are the need for addition of non-reusable coagulants and flocculants, and the production of large amounts of toxic sludge [14].

2.2.5 Membrane filtration

Membrane filtration is a collection of technologies using various kinds of membranes for treatment of wastewater [15, 17]. In ultrafiltration, a relatively low pressure forces water through the membrane and separates molecules and colloidal particles, larger than the pore size of the membrane, from the water. To make this technology useful for the removal of small mercury ions, ligands that form larger chelates with mercury are added to the water. As these ligands constitute a substantial cost, the recovery and reuse of them is necessary for ultrafiltration to be economically viable [15]. Recovery efficiencies in the range of $54 - 68\%$ have been reported.

Another membrane filtration technology, which operates under higher pressure, is reverse osmosis [15, 17]. The water passes through a semipermeable membrane and is thus separated from pollutants. Mercury removal efficiencies reported for reverse osmosis are around 83% [17]. However, the concentrated solution of pollutants that is left constitutes $20 - 30\%$ of the initial amount of water [22]. This solution is known as reject and further purification with reverse osmosis is not possible because of the high osmotic pressure.

Electro-dialysis is a membrane filtration technique specifically intended for the removal of ions [15]. Instead of pressure, the driving force for the separation is an electric field, which causes ions to move across a membrane. The membranes used in electro-dialysis are often ion exchange membranes, which will be discussed in the next section. Advantages of membrane filtration processes are their simplicity, high efficiency, metal selectivity and limited space requirement [14, 15]. Limitations of the technology are the high operational costs, low rates of water flow and problems related to clogging of the membranes. The processes are also affected by pH and the presence of other metal ions.

2.2.6 Ion exchange

Ion exchange treatment is a fast and efficient process in which mercury ions are removed from the water by exchanging them with other, harmless cations in an ion exchange resin [15, 17–19]. The ion exchange technology has attracted a lot of attention due to its ability to treat large volumes of dilute solutions of mercury ions, conditions at which most other

[1] Colloids are insoluble particles smaller than 1 μm suspended in a liquid.

wastewater treatment technologies are unable to operate. Ion exchange resins are able to reduce mercury concentrations to below 1 μg L^{-1}, and have a capacity of up to 700 mg mercury per gram of resin material [19, 23]. However, the efficiency of the ion exchange process is largely dependent on pH, temperature and contact time, and the applicability for higher concentrations of mercury is limited, as the resins are quickly saturated [14, 15, 18]. The selectivity of the technique is debated, and while a few resin types may exhibit some degree of selectivity, most conventional resins are non-selective [14, 18, 23]. The use of ion exchange resins is also limited by the high installation and maintenance costs [14]. Regeneration and reuse of the resins is often possible, by treatment with hydrochloric acid [17, 19].

2.3 Removal of mercury by electrochemical alloy formation

All of the mercury removal techniques described in the previous section have different advantages and limitations. There is currently no commercially available technology that can remove mercury efficiently in a wide range of concentrations, is unaffected by pH and the presence of other substances, does not produce large amounts of hazardous secondary waste, and that is economically and environmentally sustainable. A technique that has the potential to meet all these criteria is electrochemical alloy formation.

It is well known that liquid mercury in contact with platinum will form a platinum−mercury compound, predominantly the thermodynamically favoured alloy $PtHg_4$ [24, 25]. This alloy can also be formed by applying an electric potential to a platinum electrode in a mercury ion solution [26, 27]. Using the alloy formation of $PtHg_4$ for mercury decontamination purposes was however first suggested by Tunsu and Wickman in 2018 [4]. Mercury ions can efficiently be removed from water, by reduction and subsequent alloy formation on a thin platinum film. Electrochemical alloy formation is able to remove 99% of mercury in a wide range of initial concentrations between $0.25 - 20\ 000$ μg L^{-1} [4, 28]. It is thus effective at both high and low concentrations, and is able to remove mercury to well below the WHO and EU limits for drinking water. Another advantage is that the alloy formation and mercury removal processes are unaffected by pH in the range $0 - 6.6$ and by the presence of other metal ions in solution [4]. The capacity is very high compared to adsorption materials and ion exchange resins, being able to store over 4 000 mg mercury per gram platinum. A platinum electrode of 100 nm can be fully saturated with mercury, forming a $PtHg_4$ alloy of 760 nm, which is in good agreement with the theoretical limit. The platinum electrode can be regenerated, by reversing the potential, and then reused for further mercury removal. Mercury can be released in a small volume of solution during regeneration, ensuring easy and efficient waste management. The alloy formation process does however have very slow kinetics, requiring 130 hours to remove 90% of mercury from a 50 mL solution of 10 mg L^{-1} mercury, using a 2.25 cm^2 platinum film. One of the most important challenges to solve if this technology is to be used in industrial applications is increasing the rate of mercury removal. It has been shown that an electrode with larger surface area can increase the rate of mercury removal considerably.

Another disadvantage of the technology is the use of platinum, which is a rare and expensive metal. The platinum electrodes are reusable, nevertheless they constitute a significant installation cost, and a cheaper material is desirable for certain applications. Copper also forms an alloy with mercury, and this alloy has been investigated for mercury decontamination purposes, by using a copper electrode to remove dissolved mercury ions from solution [5]. Opposed to the platinum−mercury alloy, copper−mercury compounds form also in the absence of an applied electric potential. The potential is however necessary to stabilise the copper electrode and prevent it from dissolving. The alloy formation process between copper and mercury is significantly faster than that between platinum and mercury. The rate of mercury removal has been shown to be further enhanced by using a large surface area copper wool instead of a flat copper film as electrode. Thus, the copper−mercury system seems to be a promising alternative for mercury decontamination of water. The disadvantages compared to the platinum−mercury system is the low stability of copper and the copper−mercury alloy, and that regeneration of the copper electrode is not possible by simply reversing the potential, as for the platinum electrode. Instead, the copper−mercury alloy must be thermally decomposed to extract mercury.

3
Theory

The mercury removal technique studied in this thesis is based on electrochemistry. Therefore, Section 3.1 presents the electrochemical concepts and phenomena necessary for this project. Section 3.2 covers the theoretical background of the experimental techniques used in the project. Finally, the current knowledge of the electrochemistry and thermodynamics of the Pt−Hg alloy formation is described in Section 3.3.

3.1 Electrochemistry

Electrochemistry is a branch of physical chemistry, which has many similarities with surface physics, where the relationship between chemical processes and electricity is studied. An electrochemical cell consists of an *electrolyte*, which in this project is an acidic solution, and two or more *electrodes*, connected through an external electrical circuit [29]. The chemical reactions of interest take place at the interface between electrode and electrolyte. These reactions can either be spontaneous and produce an electrical current, or, as is the case in this project, require the supply of electrons from an externally applied electrical current. An electrochemical cell consists of two *half-reactions*, one at each of the two electrodes. At one electrode, electrons will flow from the electrode to some chemical species in the electrolyte, and such a reaction is called a *reduction* reaction. At the other electrode, an *oxidation* reaction will occur, when electrons are removed from some chemical species in the electrolyte and flow to the electrode. Electrons flow through the external electrical circuit, and the circuit is closed by ionic transfer in the electrolyte. We will now introduce some fundamental electrochemical and thermodynamic relations, before returning to practical electrochemistry.

3.1.1 Thermodynamics and electrochemical relations

An arbitrary electrochemical reaction can be written

$$\nu_A A + \nu_B B + ... + ne^- \leftrightarrows \nu_X X + \nu_Y Y + ... \tag{3.1}$$

where $A, B, ...$ are reactants, $X, Y, ...$ are products and ν_j are the stoichiometric coefficients. The Nernst equation relates the activities $a_j^{\nu_j}$ of reactants and products[1] to the potential difference between electrode and electrolyte E under electrochemical equilibrium[2]:

$$E = E^0 + \frac{RT}{nF} \ln \left(\frac{a_A^{\nu_A} a_B^{\nu_B} ...}{a_X^{\nu_X} a_Y^{\nu_Y} ...} \right) \tag{3.2}$$

[1] For a definition of the activity for various phases, see for example [30].

[2] Electrochemical equilibrium requires a balance between both chemical and electrical energies.

where E^0 is the standard potential for the reaction at hand (defined in Section 3.1.3), R the gas constant, T the temperature, n the number of electrons and F the Faraday constant [29, 30]. The electrode potential can also be related to the change in Gibbs free energy per mole ΔG of the system through

$$\Delta G = -nFE \tag{3.3}$$

The significance of Gibbs free energy in thermodynamics is that its minimum value determines the position of chemical equilibrium.

3.1.2 Three electrode systems

E in equation (3.2) is the potential difference between one electrode and the electrolyte in an electrochemical cell. This quantity can however not be experimentally determined by any measurements [30]. To measure a potential, at least two electrodes must be present, and hence we can only measure *potential differences* between two electrodes, not absolute potentials. However, many practical electrochemical systems contain three electrodes; the *working electrode* (WE), the *counter electrode* (CE) and the *reference electrode* (RE). An electrochemical cell with a three electrode system is shown in Figure 3.1. The reaction of interest is the one occurring at the WE. In the case of only two electrodes present, the second electrode serves as both CE and RE. An applied potential E_p by the potentiostat between WE and CE/RE gives the following relation between WE and CE/RE potentials:

$$E_p = E_{\mathrm{WE}} - E_{\mathrm{CE/RE}} + IR \tag{3.4}$$

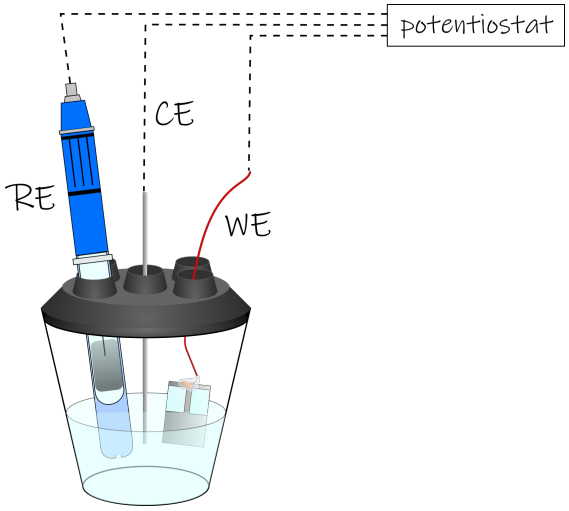

Figure 3.1: A three electrode system with a working electrode (WE), a counter electrode (CE) and a reference electrode (RE), all connected to a potentiostat.

The term IR corresponds to the electrical resistance of the electrolyte between WE and CE/RE. As a current flows through the CE/RE, chemical changes may occur and thus $E_{\mathrm{CE/RE}}$ is not a constant, but varies with activity according to the Nernst equation (3.2). It is often desirable to have a well-defined and controlled potential on the WE, and this is the reason for the introduction of the third electrode. In a three electrode system, the RE is at a fixed and well-defined potential, and the purpose of the CE is to pass the same current as

the WE. No current flows through the RE and equation (3.4) becomes

$$E_p = E_{\mathrm{WE}} - E_{\mathrm{RE}} \tag{3.5}$$

and as E_{RE} is fixed, it is possible to control E_{WE} simply by changing E_p.

3.1.3 Standard potentials and reference electrodes

We have already noted that measuring absolute potentials is impossible, and that only potential differences can be measured. Therefore, the *standard hydrogen electrode* (SHE) has been chosen as a universal reference, and all potentials in this thesis will be reported versus the SHE. The SHE consists of a Pt black electrode in a HCl solution, over which H_2 gas is bubbled [30]. At the electrode surface, the following reaction occurs:

$$2\mathrm{H}^+(\mathrm{aq}) + 2\mathrm{e}^- \leftrightarrows \mathrm{H}_2(\mathrm{g}) \tag{3.6}$$

and the electrode potential established from this equilibrium is set as the 0 of the SHE potential scale. The SHE also requires *standard conditions*, i.e. a H_2 gas pressure of 1 atm, temperature 25 °C and a H^+ concentration of 1 M. The *standard potential* E^0 of a chemical reaction is the potential measured at standard conditions and unit activity.

Using the SHE as a reference electrode in experiments is however not always practical and a wide variety of different reference electrodes are available. In this project, two different reference electrodes are used; a Ag/AgCl reference and a Hg/Hg_2SO_4 reference. The Ag/AgCl reference consists of a Ag wire immersed in a 3.0 M KCl solution [30]. The Ag wire is coated with a porous AgCl layer, and at the interface, a chemical equilibrium between these phases is established:

$$\mathrm{AgCl(s)} + \mathrm{e}^- \leftrightarrows \mathrm{Ag(s)} + \mathrm{Cl}^-(\mathrm{aq}) \tag{3.7}$$

This reaction establishes an electrode potential of $E_{\mathrm{RE,\ Ag/AgCl}} = 0.21$ V with respect to the SHE, and therefore potentials measured using this reference electrode can be converted to the SHE scale by adding 0.21 V [31].

The second reference electrode used in this project is the Hg/Hg_2SO_4 electrode, which consists of metallic Hg with a Hg_2SO_4 coating in a 0.6 M K_2SO_4 electrolyte

$$2\mathrm{Hg(s)} + \mathrm{SO}_4^{2-}(\mathrm{aq}) \leftrightarrows \mathrm{Hg_2SO_4(s)} + 2\mathrm{e}^- \tag{3.8}$$

This reaction establishes an electrode potential of $E_{\mathrm{RE,\ Hg/Hg_2SO_4}} = 0.68$ V with respect to the SHE, and potentials measured using the Hg/Hg_2SO_4 reference electrode can hence be converted to the SHE scale by adding 0.68 V to the measured value [32, 33].

The potentials measured during an electrochemical experiment will depend on temperature, pressure, electrolyte concentration and in some cases the pH of the electrolyte [30]. From the Nernst equation (3.2), the following relation can be derived for chemical reactions involving H^+ ions:

$$E = E^0 - 0.059 \cdot \mathrm{pH} \tag{3.9}$$

Since the potential determining equilibrium for the SHE, equation (3.6), involves H^+ ions, potentials measured using the SHE potential scale will be pH dependent.

3.1.4 Chronoamperometry

Chronoamperometry is an experimental electrochemical technique, in which a potential step is applied to the WE, while the current is recorded over time [29]. In this project, chronoamperometry will mainly be used to apply a constant potential, to induce alloy formation at the WE.

3.1.5 Linear sweep voltammetry

Another electrochemical technique used in this project is linear sweep voltammetry (LSV). The potential is linearly increased or decreased with time from a potential E_1 to E_2, while the current is recorded [29]. The purpose of LSV in this project is to scan the potential between different constant potentials (chronoamperometry), without having to make a potential step. It is also used to determine the potentials where certain electrochemical reactions occur.

3.1.6 Cyclic voltammetry

Cyclic voltammetry (CV) is a technique which resembles LSV. The potential is linearly scanned from E_1 to E_2, where the scanning direction is reversed, and the potential is scanned back to E_1 again [30]. The current is recorded and often displayed versus the potential in a voltammogram. A voltammogram contains information about oxidation and reduction reactions at various potentials, which will be visible as oxidation/reduction current peaks. In this project, several cycles of CV are performed to stabilise an electrodeposited platinum film. Another purpose of the CV technique is to determine the *electrochemical surface area* (ECSA) of both copper and platinum electrodes.

3.1.7 Electrochemical determination of surface area

The geometric surface area, which can be determined by macroscopic measurements, often differs from the ECSA. Some of the electrode materials considered in this project are various metal foams, with a macroscopic porosity. However, also seemingly flat surfaces can have a considerable micro-porosity, which enhances the ECSA. A useful quantity when working with surface area determination is the *roughness factor* of the surface, defined as

$$\mathrm{RF} = \frac{\mathrm{ECSA}}{A} \tag{3.10}$$

where A is the geometric surface area. Two different methods used in this project to determine the ECSA are presented below.

3.1.7.1 Hydrogen adsorption

H^+ ions will adsorb to certain metal surfaces (e.g. Pt) at a higher potential than that required for H_2 evolution [34]. In the cyclic voltammogram for Pt, this is visible as H^+ adsorption and desorption current peaks. The total charge corresponding to H^+ adsorption is found by integration of the current with respect to time. Adsorption of a full monolayer of H^+ does however overlap with H_2 evolution, thus in order to avoid contribution to the calculated charge from the H_2 evolution, only the charge corresponding to a fraction of a monolayer of H^+ is usually measured [34, 35]. It has been shown that integration of

the current to the lower H^+ adsorption current maximum corresponds to a H^+ coverage of approximately 77% [35]. The coverage at a given potential depends on whether the Pt surface is smooth or platinised, however the isotherms reported for this show relatively small deviations. Therefore a coverage of 77% will be assumed for both smooth and platinised Pt surfaces in this thesis. The relation between charge and surface area for a polycrystalline Pt surface is 210 μC cm^{-2} [34, 35], thus the ECSA can be calculated as

$$\text{ECSA} = \frac{Q}{0.77 \cdot 210\ \mu\text{C cm}^{-2}} \tag{3.11}$$

3.1.7.2 Electrical double-layer capacitance

Another way of determining the ECSA is based on the *electrical double-layer capacitance*. When applying a potential to the electrode, charge will accumulate at the interface, in the form of electrons or holes in the electrode and ions in the electrolyte [29]. This is known as the electrical double-layer. The interface between electrode and electrolyte demonstrates a behaviour similar to that of a capacitor, and the electrical double-layer is associated with a certain capacitance. The formation of an electrical double-layer is an example of a *non-faradaic process*, in which no charge transfer between electrode and electrolyte takes place. In contrast, the oxidation and reduction reactions discussed previously are *faradaic processes*.

The double-layer capacitance can be measured by performing cyclic voltammetry in a potential range with only non-faradaic processes [34, 36]. The capacitance C is related to the current I and the scan rate $\frac{dE}{dt}$ through

$$I = C\frac{dE}{dt} \tag{3.12}$$

and hence a plot of I versus $\frac{dE}{dt}$ yields a straight line with slope C. The capacitance is in turn proportional to the ECSA,

$$C = C_0 \cdot \text{ECSA} \tag{3.13}$$

where C_0 is a reference capacitance value [34]. The value of C_0 is however dependent on electrode material and experimental conditions, such as pH and electrolyte. Therefore, this method has limited use for the determination of an absolute surface area; it has however proven to be useful for comparisons between different electrodes of the same material studied under identical experimental conditions.

3.1.8 The Arrhenius equation

The rate of an electrochemical reaction can be expressed as

$$r = kc_0^n \tag{3.14}$$

where k is the rate constant, c_0 the concentration of the reactant close to the electrode surface and n the reaction order [30]. The rate constant k is often temperature dependent and follows an Arrhenius behaviour:

$$k = Ae^{-\frac{E_A}{k_B T}} \tag{3.15}$$

This is the Arrhenius equation, which relates the rate constant to activation energy E_A and temperature T. A is a pre-exponential factor and k_B the Boltzmann constant. The activation energy of a reaction can thus be determined by measuring the rate of a reaction at various temperatures, while keeping the reactant surface concentration constant.

3.2 Experimental methods

In this section, the working principles of the experimental methods used in this project are presented.

3.2.1 EQCM

The electrochemical quartz crystal microbalance (EQCM) is a method used to study electrochemical processes at a surface or interface, e.g. the formation of thin films [37]. The EQCM measures the resonance frequency, as well as the energy dissipation, of an AT-cut[3] quartz sensor. The physical phenomenon behind EQCM is the *converse piezoelectric effect*. Piezoelectricity is a material property, specific to acentric crystalline materials. When mechanical stress is applied to a piezoelectric material in a non-symmetric direction, a net dipole moment will be generated due to the displacement of charges in the crystal. This will produce an electric potential over the crystal. Conversely, when an electric potential is applied to a piezoelectric material, a mechanical strain is induced in the crystal. This is known as the converse piezoelectric effect, and is the foundation of the EQCM. An EQCM uses AT-cut quartz crystals, and due to the crystal symmetry, a shear strain is induced in the quartz crystal as a result of an applied electric potential. By applying an alternating electric potential, the quartz sensor will begin to oscillate in a shear motion. A standing acoustic wave will be established, with the quartz surfaces as antinodes. As a thin film is added to the quartz crystal, changing its thickness, the wavelength and thus the frequency is altered. The frequency shift Δf is measured and related to the mass change Δm through the Sauerbrey equation

$$\Delta f = -\frac{2f_0^2 n \Delta m}{A\sqrt{\mu_q \rho_q}} \tag{3.16}$$

where f_0 is the resonance frequency, n the overtone number, A the active area, μ_q the shear modulus and ρ_q the density of the quartz sensor.

The Sauerbrey equation is an idealised formula, only valid under certain assumptions [37]. The mass of the thin film is assumed to be less than 2% of the mass of the sensor, and the film thickness must be homogeneous. In the case of microscopic cavities present on the surface, liquid can be trapped inside the cavities, and be a significant contribution to the measured mass. From an experimental point of view, it is also interesting to note that the fundamental frequency often shows an unexpected behaviour and diverges from the overtones [38]. The reason for this is not fully understood, but likely related to the Gaussian amplitude distribution of the resonances, which is wider for the fundamental frequency, and thus may be distorted by the edges of the sensor. Therefore, measurements are often limited to the overtones.

[3] An AT-cut quartz sensor is fabricated from a quartz rod, cut at an angle of 35° with respect to the x axis.

3.2.2 PVD

Physical vapour deposition (PVD) is a collection of techniques for deposition of material on a substrate [39]. The processes used in this project are *vacuum evaporation* and *sputter deposition*. In vacuum evaporation, material from a source evaporates due to thermal heating or high energy electron beam heating and deposits on a substrate. Vacuum is necessary to prevent collision or interaction between the evaporated material and gas molecules in the chamber, and the pressure is typically in the range of 10^{-3} to 10^{-7} Pa. The sputter deposition process is based on the vaporisation of source atoms by bombardment with energetic particles. The vaporised source atoms then deposit on the substrate. Sputter deposition does not require as high quality vacuum as vacuum evaporation.

3.2.3 ICP-MS and ICP-OES

Inductively coupled plasma mass spectrometry (ICP-MS) and inductively coupled plasma optical emission spectroscopy (ICP-OES) are very sensitive tools for detection and quantification of the elements in a sample [40, 41]. A plasma of Ar ions and electrons is created, to which the sample is introduced. In the plasma, which has a temperature of $7\ 000 - 10\ 000$ K, the compounds in the sample split up into individual atoms which are then ionised. ICP-OES is based on measuring the emission spectrum from the elements in the sample, while in ICP-MS the ions are transported to a mass spectrometer, where they are separated based on their mass-to-charge ratio and detected [41]. In this way, the concentration of the different elements in the sample can be determined. The detection limit for ICP-OES is in the μg$-$mg L^{-1} range, and for ICP-MS in the ng$-\mu$g L^{-1} range.

3.2.4 SEM

Scanning electron microscopy (SEM) is an imaging and analysis tool. An electron beam is scanned over the sample to form an image [42]. The electrons in the beam interact with the sample and produce various signals, such as backscattered electrons, secondary electrons, Auger electrons and characteristic x-rays. These signals are generated by different interaction processes, and hence each signal gives a unique contribution of information about the structure and composition of the sample. In this project, SEM is used exclusively as an imaging tool.

3.3 Electrochemistry and thermodynamics of the Pt$-$Hg alloy formation

When liquid Hg is in contact with Pt, or when a sufficient negative potential is applied to a Pt electrode in an electrolyte containing Hg^{2+} ions, a compound is formed [24, 27, 43]. $PtHg_4$ is the dominating phase, however PtHg and $PtHg_2$ have also been reported [26, 44]. The overall chemical reaction for the electrochemical alloy formation of $PtHg_4$ is the following:

$$Pt(s) + 4Hg^{2+}(aq) + 8e^- \rightarrow PtHg_4(s) \tag{3.17}$$

The reaction is however likely divided into several sub-reactions and sub-steps, where PtHg and $PtHg_2$ may form as intermediate compounds [4]. The main sub-steps of the reaction

are:

1. The reduction of a Hg^{2+} ion.

$$Hg^{2+} + 2e^- \rightarrow Hg^0 \tag{3.18}$$

2. The diffusion of the Hg^0 atom through the $PtHg_4$ alloy.
3. The insertion of the Hg^0 atom into the Pt lattice, and formation of the $PtHg_4$ alloy at the Pt-alloy interface.

The kinetics of this reaction has been studied using EQCM, showing that the rate of alloy formation is constant over time, which indicates that the diffusion of Hg atoms through the alloy is fast compared to other steps of the reaction [45].

The activation energy of the alloy formation for the Pt−liquid Hg system has been reported in two different articles, and the values differ quite substantially: 0.35 and 0.52 eV [24, 25]. For the electrochemical alloy formation between Pt and Hg, the activation energy has been determined to be 0.35 eV by measurements of the temperature dependence of the rate of alloy formation in the range $20 - 40$ °C, using EQCM [45]. One of the aims of this study is to improve on the certainty of this value, by performing repeated measurements at each temperature as well as extending the temperature range.

4
Methods

In this chapter, the experimental method is described and the details about all materials and experiments are presented. The focus of Section 4.1 is the electrodes and electrode fabrication processes. The experimental setup and methodology for EQCM measurements is the topic of Section 4.2. Measurements of the ECSA are presented in Section 4.3 and details about the batch experiments performed are given in Section 4.4.

4.1 Electrodes

Several different types of electrodes are used in the experiments in this thesis. While the active material is either Pt or Cu, a few other materials serve as substrates. All WE used are listed in this section, and the fabrication and preparation processes are described.

4.1.1 PVD Pt thin-film electrodes

In this section, thin-film electrodes fabricated by either of the PVD processes vacuum evaporation and sputter deposition are presented. The electrodes consist of a substrate onto which a few hundred nm of Pt is deposited.

4.1.1.1 Pt thin-film on glass

The purpose of Pt thin-film electrodes on glass is to serve as a comparison to larger surface area electrodes, as this design provides a well defined surface area. The substrate is a 0.5 mm thick, polished fused silica glass wafer, which was cut into pieces of 30 mm x 15 mm by the use of a dicing saw (Loadpoint Microace 3+). Prior to the deposition of material, the glass pieces were cleaned in an ultrasonic bath: first 10 minutes in acetone, then 10 minutes in pure water and finally 10 minutes in isopropyl alcohol. A 3 nm Ti film followed by a 100 nm Pt film was deposited on the glass pieces by a vacuum evaporation system (Lesker PVD 225). The purpose of the Ti layer is to ensure better adhesion of Pt to glass. A deposition mask was used to create the pattern shown in Figure 4.1, consisting of a 15 mm x 15 mm Ti + Pt square connected to the top of the electrode by a 1 mm connection strip. The 15 mm x 15

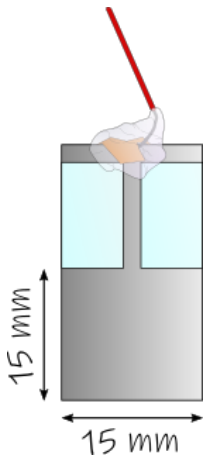

Figure 4.1: A Pt thin-film electrode, consisting of a 30 mm x 15 mm fused silica glass, onto which 3 nm Ti and 100 nm Pt are deposited.

mm square provides an active area of 2.25 cm^2,[1] and the electrolyte level was fixed just above the square during all experiments. Electrical contact at the top of the electrode was established by connecting a Cu wire with conductive Cu tape to the Pt contact region. The connection was sealed with hot glue to prevent leakage of Cu into the electrolyte.

4.1.1.2 Quartz sensors

The WE for EQCM measurements are planar AT-cut quartz sensors, with thickness 0.3 mm, diameter 14 mm and resonant frequency 4.95 MHz ± 50 kHz (LAB Analytical, Sweden). Prior to the deposition of Pt, the sensors were cleaned using the same procedure as described for the silica glass pieces in Section 4.1.1.1. Using a deposition mask, a 200 nm Pt layer on top of a 3 nm Ti layer was evaporated using the same method as in Section 4.1.1.1. The deposited pattern consists of a circle with diameter 5 mm, connected to the Au electrode on the other side of the sensor by a 1 mm strip, see Figure 4.2.

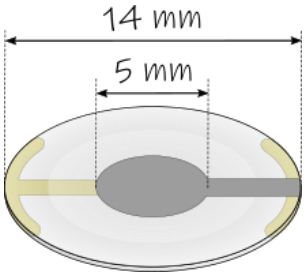

Figure 4.2: A quartz sensor with a 5 mm diameter Pt front electrode and a 1 mm connector strip, deposited by evaporation.

4.1.1.3 Electrodes fabricated by Pt sputter deposition

A PVD sputter system (NORDIKO 2000 sputter) was used to sputter 200 nm Pt onto two different substrates: a stainless steel (SS316L) sheet and a Ti fibrous substrate. These electrodes were used in the case studies presented in Section 6.1 and 6.2. A Cu wire was attached to the top of the SS316L electrode using conductive Cu tape and the connection was sealed with hot glue. For the Ti fibrous electrode, electrical contact was established by welding a thin Ti metal strip to the electrode.

4.1.2 Pt black electrodes

To obtain a Pt electrode with a larger ECSA, porous Pt black was electrodeposited on some SS316L sheets. An electrolyte was prepared by mixing 3 g $H_2PtCl_6 \cdot 6\ H_2O$ with 100 mL 0.5 M H_2SO_4. The experimental setup for electrodeposition of Pt black on a SS316L sheet is shown in Figure 4.3. The SS316L sheet has dimensions 10 mm x 40 mm, and the electrolyte level was fixed 20 mm from the top of the electrode. Thus, the active area is 4.0 cm^2, as both sides of the sheet are active. Electrical contact was established by the attachment of a Cu wire to the top of the electrode, and the connection was sealed with hot glue. The SS316L electrode was connected as WE, a Pt wire as CE and a Ag/AgCl electrode was used as RE. A constant current density of -45 mA cm^{-2} was applied to the WE for 140 s using a Gamry Reference 600 potentiostat. During this electrodeposition process, a black coating appears on the WE, which indicates that the deposition of Pt black has been successful.

The electrodes were stored in Milli-Q over night, after which the Pt black layer was stabilised by an aging procedure. Aging was performed in 0.5 M H_2SO_4, with a Pt wire as CE and a

[1] This area may vary due to manual placement of the tape used as deposition mask, and the geometric surface area of each electrode is therefore measured prior to every experiment.

Ag/AgCl electrode as RE. Using a Gamry Reference 600 potentiostat, CV was performed for 500 cycles between 0−1.4 V, at a sweep rate of 100 mV s^{-1}. The electrodes can then be stored in Milli-Q for several weeks without degradation until being used in experiments.

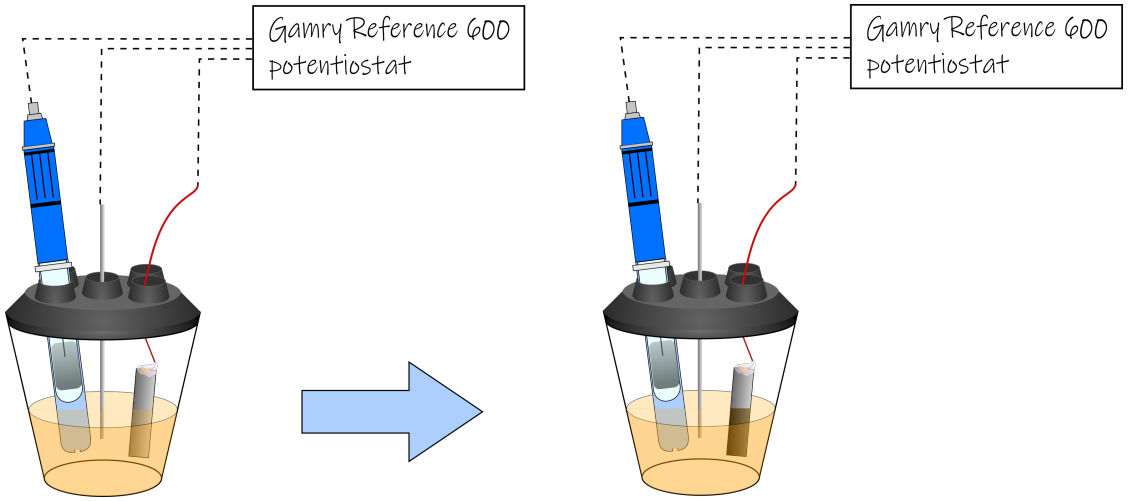

Figure 4.3: The experimental setup for electrodeposition of Pt black on a SS316L substrate from a H_2PtCl_6 solution.

4.1.3 Metal sheet and metal foam electrodes

A few different metal sheet and foam electrodes were also used in the experiments. For the investigations of the Cu−Hg alloy formation, both Cu sheets and Cu foams were used. The Cu foams were cut in pieces of 25 mm x 15 mm x 10 mm and had an average pore size of 0.5±0.2 mm, shown in Figure 4.4. Electrical contact for the Cu sheets was established in the same way as for the SS316L sheets, while electrical contact for Cu foams was established by soldering the Cu wire to the top of the foam. During experiments, the electrolyte level was fixed 2−3 mm below the soldering point.

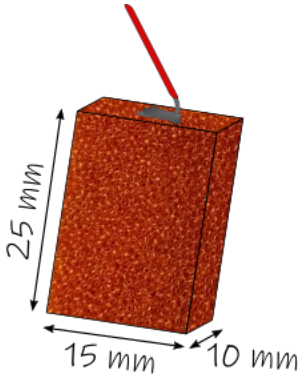

Figure 4.4: The Cu foam electrode.

Another electrode material used is Ti foams with an average pore size of 1.4±0.3 mm and thickness 15 mm. The Ti foams had been pre-treated to prevent oxidation and then platinised with 2 μm Pt at Magneto Special Anodes. Three different foams were provided: A) No etching, B) Etched for 5 minutes, and C) Etched for 10 minutes. Electrical contact was established by welding a piece of the Ti foam to a thin strip of a Ti sheet.

SS316L foams with a thickness of 3 mm and average pore size of 0.6±0.1 mm, were also used as electrode material. The foams were platinised with 1−2 μm Pt by Umicore through a high temperature electrolysis process in a molten salt solution. Electrical contact was established by twining a thin SS316L wire with the foam.

4.2 EQCM

The temperature dependence of the alloy formation between Pt and Hg was studied by performing EQCM measurements. The experimental setup is shown in Figure 4.5 and consists of a three electrode system with a Hg/Hg_2SO_4 RE, a Pt wire as the CE and the Pt film on the quartz sensor as the WE. Before each measurement, the quartz sensor was cleaned in an ultrasonic bath: first 5 minutes in acetone, then rinsed with Milli-Q, followed by 5 minutes in isopropyl alcohol. Finally the sensor was again rinsed with Milli-Q and blown dry with N_2 gas. The quartz sensor was mounted in a Microvacuum QSH dip sensor holder immersed in the electrolyte. The electrolyte was 50 mL 0.5 M H_2SO_4 with 10 mg L^{-1} Hg^{2+}. The concentration of Hg^{2+} was high enough compared to the area of the WE and the time of the experiments, that it can be assumed constant throughout each experiment. During an experiment, the solution was stirred using a magnetic stirrer, as this proved to be important during initial testing. Without stirring, the rate of alloy formation measured was not constant over time, which is in contrast to earlier studies [45]. This proves that the alloy formation, at least to some extent, is limited by the diffusion of Hg^{2+} ions in solution. At the start of the experiment, the potential was set to 0.73 V using a Biologic SP300 potentiostat. This potential was chosen as a stable potential where no alloy formation should occur. The potential was then scanned to 0.18 V to induce alloy formation. At the end of the experiment, the potential was scanned back to 0.73 V. During the experiment, the resonance frequency of the quartz sensor and several overtones were recorded by a QSense Analyzer. The experiments were performed at different temperatures between $20 - 60$ °C. The temperature was controlled using a water bath (Julabo F12-ED) connected to a thermostated glass vessel, in which the electrolyte was contained. At 20 °C, 7 experiments were performed, at 60 °C, 4 experiments were performed, at 30 and 50 °C, 3 experiments were performed and at 40 °C, 2 experiments were performed.

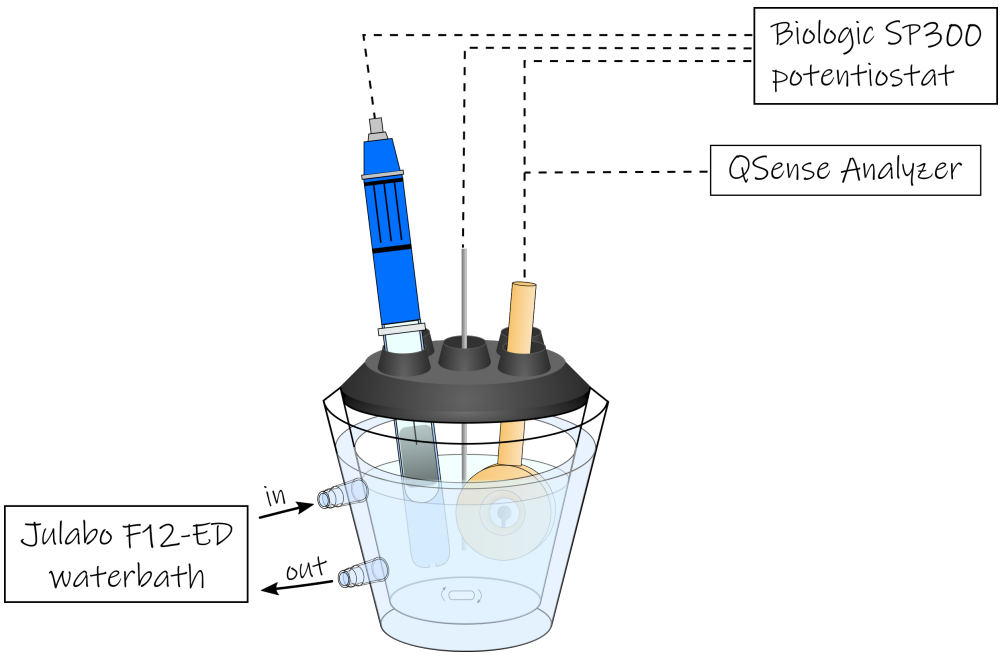

Figure 4.5: The experimental setup for the EQCM experiments. The setup consists of a three electrode system, with a Hg/Hg_2SO_4 RE, a Pt wire as CE and a quartz sensor as the WE.

4.3 ECSA measurements

Measurements of the ECSA of the electrode materials used in this project were performed using the two methods presented in Section 3.1.7. For WE coated with Pt, the hydrogen adsorption method is used, and for WE made of Cu, the electrical double layer capacitance is measured. All ECSA measurements were performed using a three electrode system, with a Pt wire as CE. The electrolyte was bubbled with Ar gas for 10 minutes prior to the measurements.

4.3.1 Hydrogen adsorption on Pt surfaces

The experimental setup for determination of the ECSA of a Pt surface is shown in Figure 4.6. The setup consists of a Pt wire CE, a RE and a WE. This experiment was performed to determine the ECSA of three different electrodes: the Pt thin-film electrodes (shown in Figure 4.6), the Pt black electrodes and the Pt coated Ti foam electrodes. The setup and procedure for the experiments was identical, except that a Ag/AgCl RE was used for the Pt black and Ti foam electrodes, while a Hg/Hg_2SO_4 RE was used for the Pt thin-film electrodes. The electrolyte was 0.5 M H_2SO_4 and a CV was recorded in the potential range $0 - 1.4$ V. The scan rate for the Pt thin-film electrodes was 50 mV s^{-1}, for the Pt black electrodes 100 mV s^{-1} and for the Pt coated Ti foam electrodes 5 mV s^{-1}.

The current was integrated in the potential range corresponding to H^+ adsorption, as described in Section 3.1.7, and divided by the scan rate to obtain the total charge. The ECSA was then calculated using equation (3.11). Finally, the RF of the electrode could be found through equation (3.10).

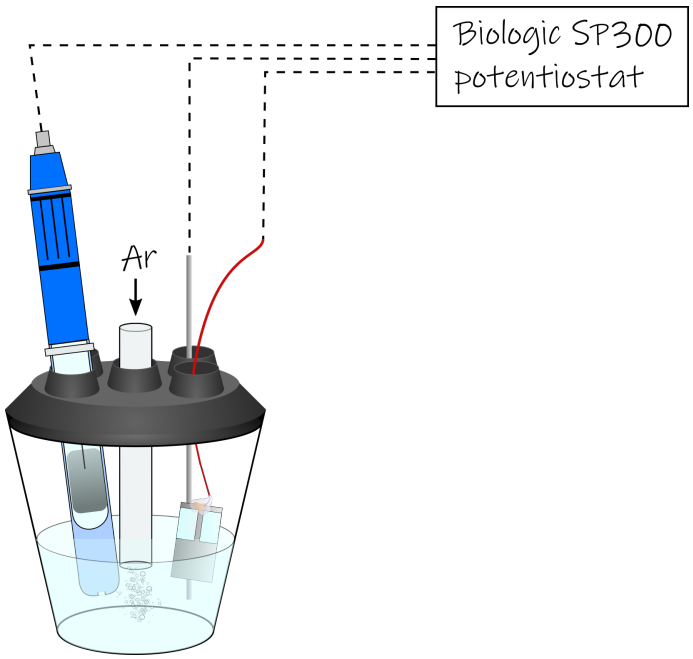

Figure 4.6: The experimental setup for measurement of the hydrogen adsorption on a Pt thin-film electrode. The setup consists of a three electrode system with a Hg/Hg_2SO_4 RE, a Pt wire as CE and the Pt thin-film electrode connected as WE. Ar gas is bubbled into the 0.5 M H_2SO_4 electrolyte.

4.3.2 Capacitance measurements on Cu surfaces

Capacitance measurements on Cu electrodes were performed in 0.1 M KOH electrolyte. The experimental setup was similar to that in Figure 4.6, with a Hg/Hg_2SO_4 RE and a Cu WE. Capacitance measurements were performed for both the Cu sheet and Cu foam electrodes. Prior to the measurement, the electrodes were quickly immersed in 0.5 M H_2SO_4 to remove any Cu oxide from the surface. At first, a CV was recorded in a wide potential range to identify a suitable measurement range dominated by non-faradaic processes. The potential range chosen was -0.4−-0.1 V, and in this range CV:s were recorded at scan rates between 50 and 300 mV s^{-1}.

The current was plotted versus the scan rate, and the capacitance could thus be determined using equation (3.12). As the reference capacitance value in equation (3.13) is highly dependent on the experimental conditions, no tabulated value of C_0 was used. Instead, equation (3.13) was used to determine the ratio of ECSA between the Cu foam and Cu sheet.

4.4 Batch experiments

The Hg^{2+} removal efficiency of each electrode material was evaluated by performing batch experiments. All batch experiments were performed in 50 mL of electrolyte, and using a three electrode system. Before each experiment, all glassware were cleaned by the following procedure, to reduce the risk for contamination. The glassware were first soaked in concentrated H_2SO_4 for a few hours, after which they were rinsed with Milli-Q five times and blown dry with N_2 gas. At the start of a batch experiment, the potential was quickly scanned using LSV, with a scan rate of 100 mV s^{-1}, to a fixed potential where alloy formation occurs and kept constant during the rest of the experiment, using chronoamperometry. A magnetic stirrer was used to stir the electrolyte during all experiments. Before, during and after the experiments, samples were taken from the electrolyte for ICP-MS and ICP-OES analysis. The amount of electrolyte in each sample and the time between samples varies between the different experiments. The samples were diluted to achieve a Hg^{2+} concentration around $10 - 20$ μg L^{-1} in the initial sample, so that the concentration of all samples were within the ideal detection range of the ICP-MS. Initially, the samples were diluted using 0.5 M HCl with an internal standard of 2 μg L^{-1} In, however halfway through the project it was decided to switch to 1 M HCl with an internal standard of 2 μg L^{-1} Bi. This was due to the occurrence of many elements in the samples with an atomic mass number close to that of In, which caused a disturbance in the ICP-MS analysis. The specifics of each batch experiment are presented below.

4.4.1 Batch experiments with Cu electrodes

The electrolytes for batch experiments with Cu WE were tap water, with an initial concentration of 100 μg L^{-1} Hg^{2+}. Tap water was used as Cu dissolves in acidic electrolytes, and the intention was also to get as close as possible to the conditions of the intended application of Cu electrodes, which is the removal of Hg from dental clinics' wastewater. The CE was a Pt wire, the RE was a Ag/AgCl electrode and the potential was set to -0.19 V. Two different experiments with Cu electrodes were performed; one using a Cu sheet and one using a Cu foam as WE. Prior to the experiment, the Cu foam was cleaned in isopropyl alcohol for 5

minutes in an ultrasonic bath, to remove a layer of antioxidant coating from the supplier. The Cu foam was then thoroughly rinsed with Milli-Q and blown dry with N_2 gas. The Cu sheet did not have an antioxidant coating. Both electrodes were however quickly cleaned with 0.5 M H_2SO_4, before immersion into the electrolyte, in order to remove any Cu oxide on the surface. The first sample of the Cu batch experiments was taken before the Cu electrode was immersed in the solution. The potential was applied immediately after lowering the electrode into the electrolyte, to avoid any dissolution of the Cu electrode. The Hg^{2+} concentration in the samples taken from the electrolyte was analysed using ICP-MS. The concentration of Cu in the Cu foam experiment was also analysed using ICP-MS, while the Cu concentration in the Cu sheet experiment was analysed using ICP-OES.

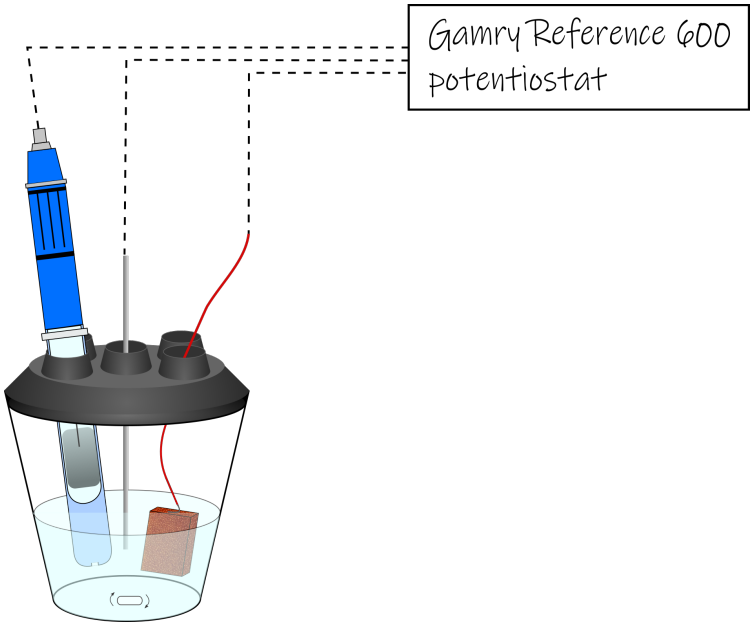

Figure 4.7: The experimental setup for removal of Hg^{2+} from tap water, using a Cu foam WE. The setup consists of a three electrode system with a Ag/AgCl RE and a Pt wire as CE. A Gamry Reference 600 potentiostat is used to apply -0.19 V to the WE.

4.4.2 Batch experiments with Pt electrodes

The batch experiments with Pt electrodes were performed in 0.5 M H_2SO_4 with an initial concentration of 500 μg L^{-1} Hg^{2+}. Five different batch experiments with Pt electrodes were performed: one using a Pt thin-film WE, one using a Pt black WE and three using the Pt coated Ti foams A, B and C, described in Section 4.1.3. The experimental setup for the Pt thin-film electrode is shown in Figure 4.8, and consists of a three electrode system with an Ag/AgCl RE and a Pt wire CE. The potential was set to 0.18 V. The setup for all five experiments was identical, except that a Hg/Hg_2SO_4 RE was used for Ti foam B. The concentration of Hg^{2+} in the samples taken before, during and after the experiments was analysed by ICP-MS.

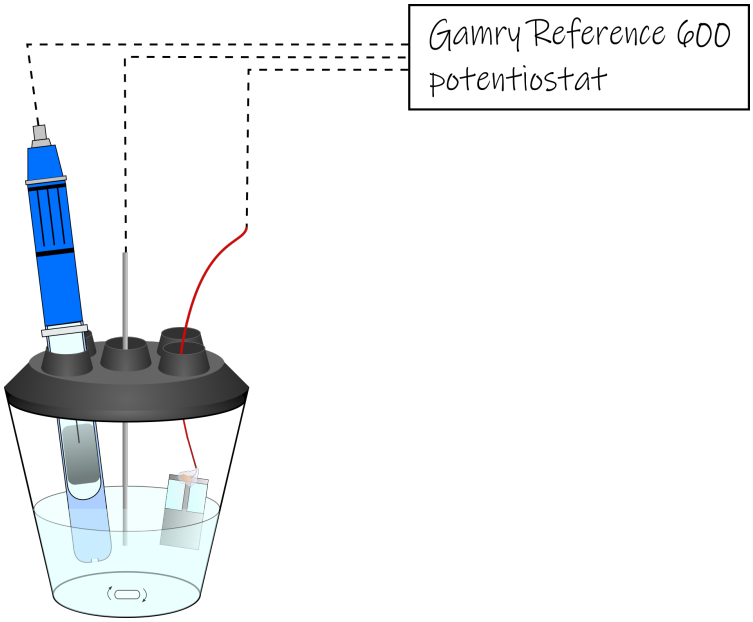

Figure 4.8: The experimental setup for removal of Hg^{2+} from 0.5 M H_2SO_4, using a Pt thin-film WE. The setup consists of a three electrode system with a Ag/AgCl RE and a Pt wire as CE. A Gamry Reference 600 potentiostat is used to apply 0.18 V to the WE.

5

Results and discussion

In this chapter, the results from all experiments described in Chapter 4 are presented. Section 5.1 addresses the temperature dependence of the Pt−Hg alloy formation, studied by EQCM measurements. The activation energy of the reaction is determined in Section 5.1.1, and a MATLAB model based on the activation energy is briefly described in Section 5.1.2. In Section 5.1.3, the activation energy determined in this thesis is compared with previous studies of the Pt−Hg system. The focus of the thesis is then shifted to investigating the relation between surface area and structure of the electrode, and the rate of alloy formation in Section 5.2. This section is divided into two separate parts, Section 5.2.1, where Cu electrodes are studied and 5.2.2 where Pt electrodes are studied. The ECSA of the Cu electrodes, measured by the electrical double layer capacitance, is compared to the Hg^{2+} removal rates. Correspondingly for the Pt electrodes, the ECSA, measured by H^+ adsorption, is compared to the Hg^{2+} removal rates.

5.1 Temperature dependence of the Pt−Hg alloy formation

The alloy formation between Pt and Hg was studied by performing EQCM measurements at 20, 30, 40, 50 and 60 °C, as described in Section 4.2. The frequency shift measured by EQCM could then be related to the increase in mass on the sensor through the Sauerbrey equation (3.16). Mass shifts versus time of the experiment are visualised in Figure 5.1, with one representative experiment shown for each temperature. The 3rd, 5th and 7th harmonics are displayed for each experiment. The mass begins to increase as the potential is set to 0.18 V, and corresponds to the amount of Hg taken up on the WE through alloy formation. Note that the scale differs between the different experiments in Figure 5.1, and that the mass increase is faster at higher temperatures. It can also be noted that the harmonics tend to diverge with time, an effect which is more pronounced at higher temperatures. This indicates some degree of inhomogeneity of the alloy layer formed, as the harmonics measure slightly different areas of the sensor. The deviation between the 3rd and 7th harmonics at the end of the experiment at 60 °C is 16% and at 20 °C only 1%. As the deviation is small, the alloy layer formed is still largely homogeneous over the Pt coated area of the sensor. This reasoning applies to a homogeneity over the relatively large scale of the entire sensor, and these measurements do not give any information about the local structure of the alloy. However, the larger deviation at higher temperatures might be an indication that the alloy formed under these conditions is less homogeneous than alloys formed at room temperature.

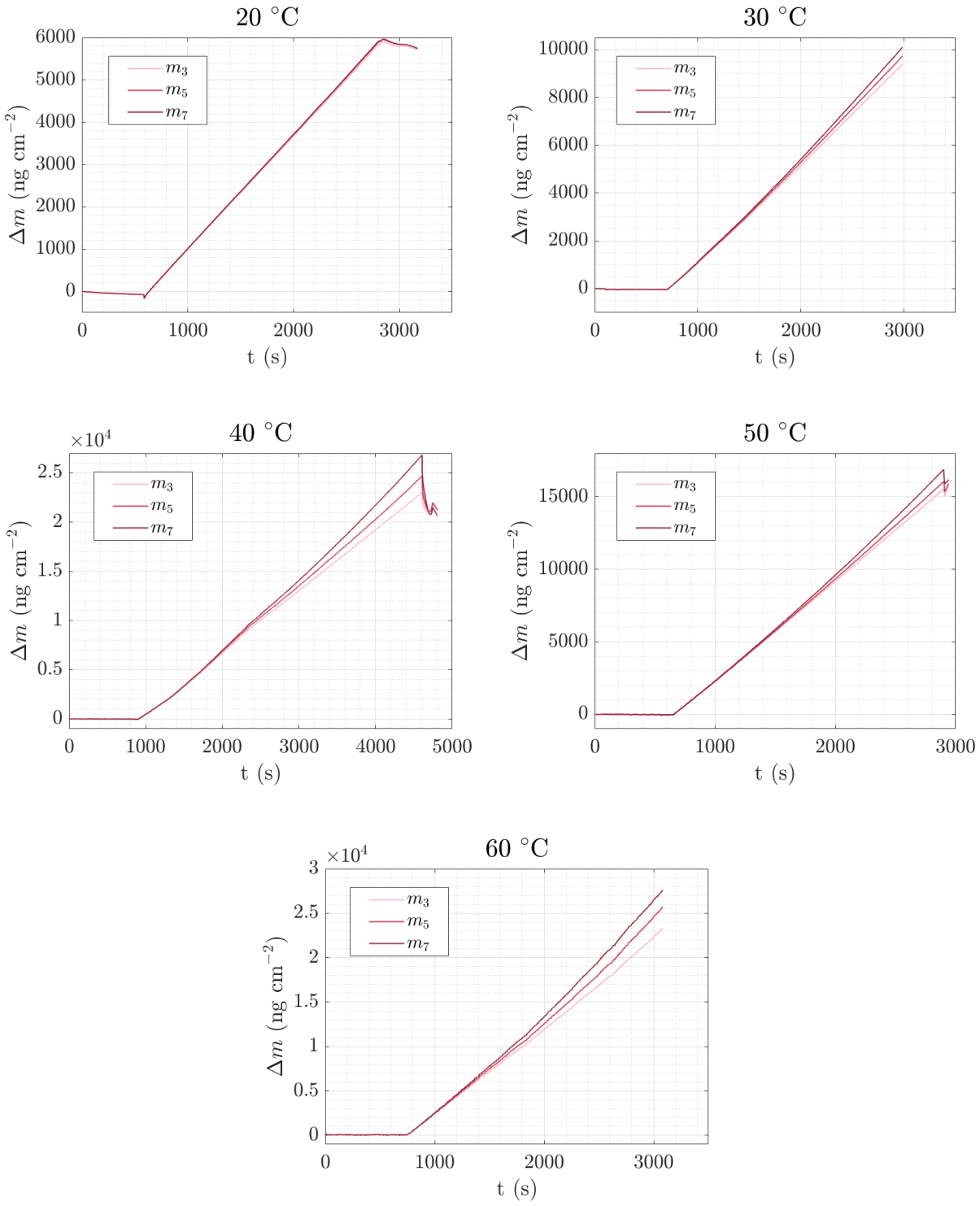

Figure 5.1: Mass shifts, Δm, calculated using the Sauerbrey equation, from the frequency shifts, Δf, measured with EQCM during alloy formation between Pt and Hg. The mass shifts corresponding to the 3rd, 5th and 7th harmonics are shown for temperatures 20−60 °C.

5.1.1 Activation energy of the Pt−Hg alloy formation

To determine the apparent activation energy of the alloy formation between Pt and Hg, we rewrite the Arrhenius equation (3.15) as

$$\ln k = \ln A - \frac{E_A}{k_B} \cdot \frac{1}{T} \tag{5.1}$$

Thus, a plot of $\ln k$ versus $\frac{1}{T}$ would allow determination of the activation energy E_A of the reaction. The rate constant k was not directly measured in this project, however the rate of alloy formation is given by the slope of each harmonic in Figure 5.1. For an experiment with constant concentration, which is assumed in this case[1], the rate is simply proportional to the rate constant, and does not change over time, see equation (3.14). The activation energy can thus instead be determined from a plot of the logarithm of the rate versus the inverse temperature. Such a plot, an Arrhenius plot, is shown in Figure 5.2, where the mean and standard deviation of the rate are calculated from harmonics 3, 5 and 7 of all measurements. The slope of a linear fit to the data is -3 351 K, which corresponds to an activation energy of 0.29 eV.

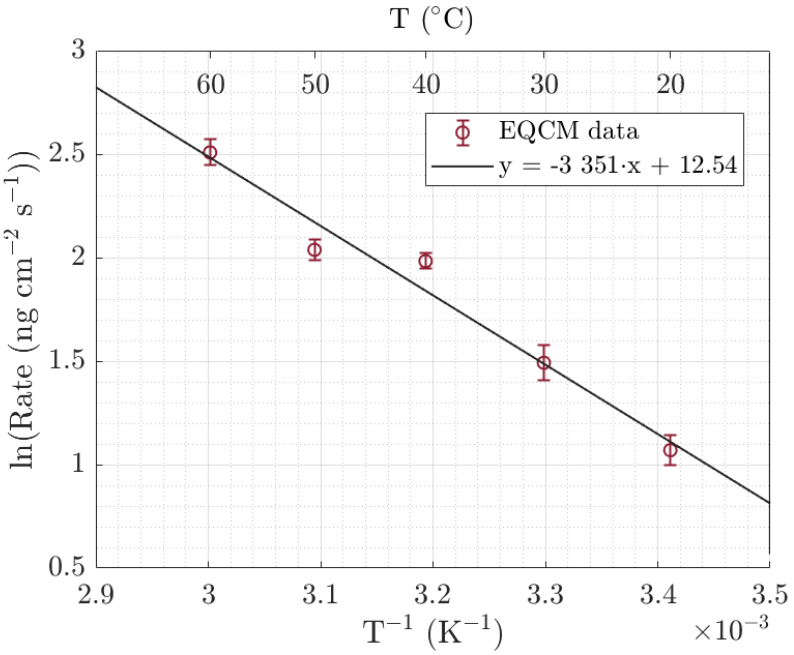

Figure 5.2: Arrhenius plot showing the logarithm of the measured alloy formation rate for temperatures 20 − 60 °C. A linear fit to the data is also shown.

5.1.2 MATLAB model for Hg^{2+} removal

The activation energy determined in this work, together with a study of the Hg^{2+} removal rate as a function of concentration [28], was used to construct a MATLAB model for predictions of the Hg^{2+} removal from solution using Pt electrodes. Input parameters to the model are the initial Hg^{2+} concentration, electrode surface area and temperature, from which the model estimates the Hg^{2+} concentration in solution over time of the experiment. The construction of the MATLAB model was not a part of this thesis; it is however used in the

[1]Regular ICP-MS analysis of the electrolyte confirmed this assumption as reasonable.

following sections for comparisons with the Hg^{2+} removal rates in experiments. Specifically, it has been used to determine the equivalent active surface area from comparisons with experimental data.

5.1.3 Comparison with previous studies of the Pt−Hg system

Relatively few studies have investigated the kinetics of the Pt−Hg system, and to the best knowledge of the author of this thesis, only one previous study has attempted to determine the activation energy of the alloy formation between solid Pt and Hg^{2+} ions in solution. In this study, the activation energy was determined to 0.35 eV, also using EQCM as the experimental method [45]. However, the experimental setup of the previous study differs from that of the current one. The measurements were performed using a QSense Electrochemistry module and flowing electrolytes, in contrast to the QSH dip sensor holder used in the current study. In addition to this, the previous study was based on one experiment only at each of the temperatures 20, 30 and 40 °C, while the current study extends to 60 °C and is based on 19 experiments in total. The activation energy of 0.29 eV found in this study agrees rather well with the 0.35 eV of the previous one, and thus, these studies largely confirm each other. More confidence should however be placed in the value determined in this thesis, as it is based on repeated measurements and extends to a larger temperature range.

Another interesting comparison to make is with the activation energy of the Pt−liquid Hg system. Two studies have attempted to measure the activation energy of this system. Both studies employ a gravimetric technique and report values of 0.35 and 0.52 eV, respectively, for the activation energy [24, 25]. Despite studying the same system, the reaction rates measured differ with a factor of 20. Thus, there is a significant uncertainty in the activation energy for the Pt−liquid Hg system. However, interestingly, the lower of the reported values is in rather good agreement with the activation energy for the Pt−Hg^{2+} ion system, which may indicate a similar reaction mechanism and rate determining step of alloy formation in the Pt−liquid Hg system and the Pt−Hg^{2+} ion system.

5.2 Relating the electrode surface area and structure to the rate of alloy formation

In this section, the electrode structure and surface area are compared with the rate of alloy formation. Understanding how the reaction rate scales with electrode surface area, and how the structure of the electrode affects the Hg^{2+} removal rate, is of great importance when designing electrodes for applications of this technology. Section 5.2.1 addresses Cu electrodes, while Pt electrodes are treated in Section 5.2.2.

5.2.1 Cu electrodes

The low abundance and high cost of Pt makes it impractical for certain applications, where the price is a limiting factor. A cheaper alternative is Cu, which is also known to form an alloy with Hg [5]. However, the prospects of using Cu as electrode material for Hg removal is largely dependent on the pH of the solutions in need of decontamination. Cu dissolves

in acidic electrolytes, which rules out many industrial wastewaters with low pH. Currently, the main application envisaged for Cu electrodes is the removal of Hg from dental clinics' wastewater. Increasing the rate of alloy formation, compared to previous studies [5], is vital to be able to meet the relatively large water flow rates out from the dental clinics. In this section, we measure the rate of Hg^{2+} removal for two different Cu electrodes, and investigate how the reaction rate scales with ECSA.

5.2.1.1 Determination of ECSA of Cu electrodes

We begin this section with determining the ECSA of the Cu sheet and Cu foam electrodes, through measurements of the electrical double-layer capacitance, as described in Section 4.3.2. Figure 5.3 shows a representative example of one cycle from the CV of the Cu sheet and the Cu foam. Ideally, a purely capacitive CV should be centred around 0 A. As can be seen in Figure 5.3, both CV curves are off centre, and slightly tilted, something that is probably caused by the presence of H_2 and O_2 in the electrolyte. The electrolytes were bubbled with Ar gas in order to obtain as well centred CV curves as possible, however this does not appear to have been completely effective. Thus, the current measured is not exclusively generated by non-faradaic processes. However, as the aim primarily was to obtain an estimate of the ECSA, these measurements are deemed sufficient.

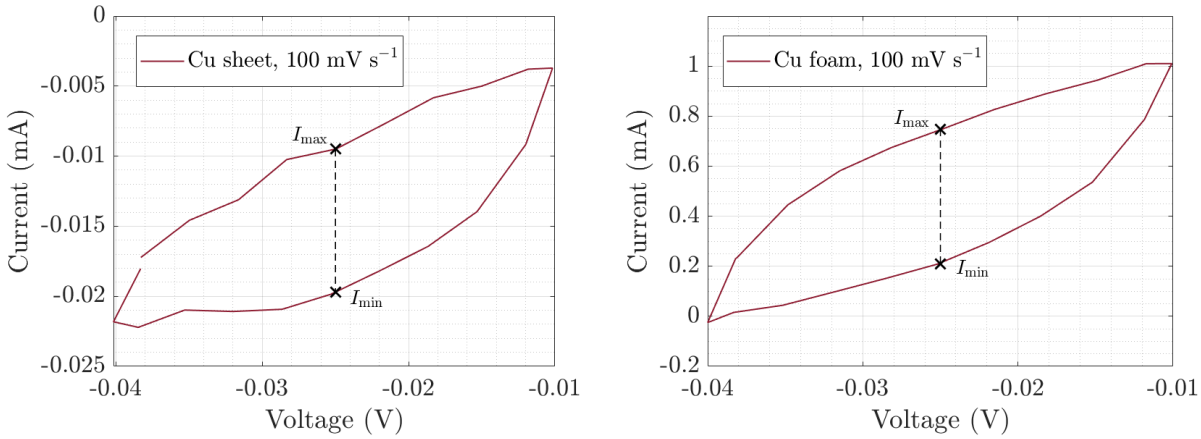

Figure 5.3: One representative cycle from the CV of the Cu sheet (left) and the Cu foam (right).

The maximum current I_{max} and the minimum current I_{min} at the centre voltage -0.025 V can be found from the CV curves in Figure 5.3. The current I in equation (3.12) is thus given by

$$I = \frac{I_{\text{max}} - I_{\text{min}}}{2} \tag{5.2}$$

The current density J is then calculated by normalising I to the geometric surface area of the electrode. For the Cu sheet, this area is unambiguous, while the choice of a reasonable geometric surface area for the foam is less obvious. Here, the current has been normalised to the geometric area of the largest side of the foam, in order to obtain the ECSA per cm^2 of the foam (as the foam has a thickness of 1 cm). Repeating this for each scan rate, and plotting the current density J versus the scan rate $\frac{dE}{dt}$, produces Figure 5.4. Note that only scan rates up to 125 mV s^{-1} are shown for the Cu foam, as non-ideal effects became significant in the CV at larger scan rates. This effect is more pronounced for the foam, due to the

larger ECSA. A straight line is fitted to each set of data in Figure 5.4, and the capacitance C is determined as the slope of the line, according to equation (3.12). Ideally, if only non-faradaic processes were contributing to the measured current, the current density would be directly proportional to the scan rate. As can be seen in Figure 5.4, the data for the Cu sheet closely follows a direct proportionality, and thus, the faradaic contribution is almost negligible. However, the faradaic contributions are not negligible for the Cu foam, which can be seen from the relatively large constant in the linear fit. The faradaic contributions are also dependent on the scan rate, and thus, introduce an error to the determination of the capacitance from the slope of the line.

The capacitance of the Cu sheet is determined to $C_{\text{sheet}} = 6.91 \cdot 10^{-6}$ F cm^{-2} and of the Cu foam $C_{\text{foam}} = 3.38 \cdot 10^{-4}$ F cm^{-2}. We can now calculate the ratio between the ECSA of the foam and sheet using equation (3.13):

$$\frac{\text{ECSA}_{\text{foam}}}{\text{ECSA}_{\text{sheet}}} = \frac{C_{\text{foam}}}{C_{\text{sheet}}} \approx 49 \tag{5.3}$$

The significance of this number is that the ECSA of 1 cm^2 (or, equally, 1 cm^3) of the Cu foam is 49 times larger than the ECSA of 1 cm^2 of the Cu sheet. If we assume that the surface of the Cu sheet and Cu foam have similar structures and roughness, the Cu foam has an equivalent area of 49 cm^2 cm^{-3}.[2] This value can be compared with tabulated values of the surface area of metal foams, based on the average pore size. The tabulated value of the surface area of a metal foam with average pore size 0.5 mm is 50 cm^2 cm^{-3}, which is in excellent agreement with the value measured here [46].

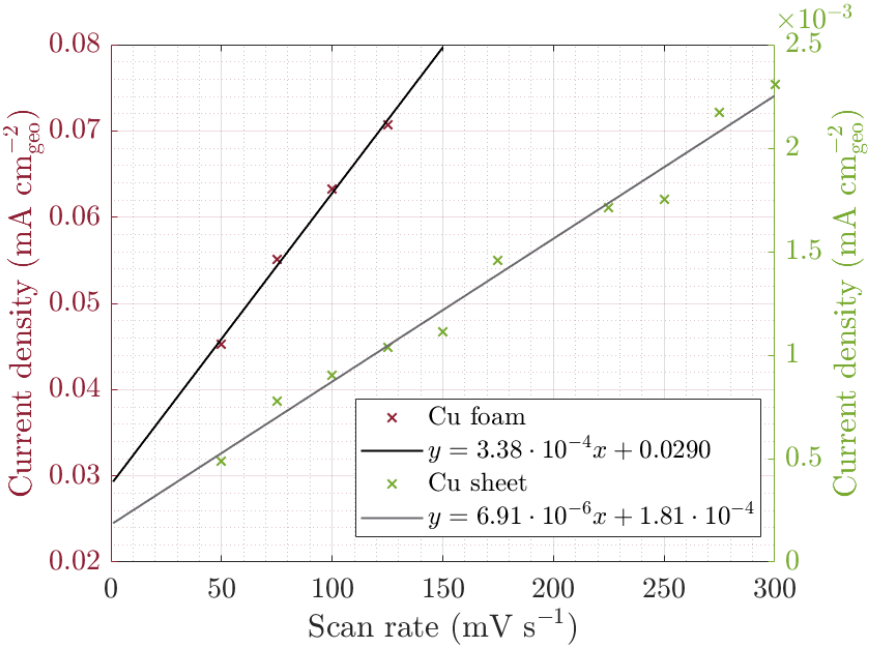

Figure 5.4: Current density J versus scan rate $\frac{dE}{dt}$ for the Cu foam and Cu sheet electrodes. A linear fit to each set of data is also shown.

[2]Note that this is not the ECSA, but rather a measure of the area of the pores, i.e. not on the atomic level.

5.2.1.2 Hg^{2+} removal from tap water using Cu electrodes

We now move on to the Hg^{2+} removal efficiency of the Cu electrodes, determined by the experiments described in Section 4.4.1. The results from the ICP-MS and ICP-OES analysis of the electrolyte from the Hg^{2+} removal experiment with a Cu sheet electrode are shown in Figure 5.5. The concentration of Hg^{2+} decreases over time, while the concentration of Cu is relatively constant throughout the experiment. In this experiment, a few, possibly significant, sources of error were present. For a better understanding of these issues and the cause of them, a short explanation of the ICP-MS analysis procedure will be provided. Before each measurement, the instrument is calibrated using a series of standard samples, with known concentration of Hg^{2+}. Based on these standard samples, the intensity of Hg measured by the instrument can be translated to a concentration in μg L^{-1} Hg^{2+}. For this particular analysis, the calibration did not generate reasonable results, e.g. the standard sample with 50 μg L^{-1} Hg^{2+} contained less than 3 times as much Hg as the 10 μg L^{-1} Hg^{2+} standard sample. The reason for this is unknown, but may be due to inexact pipetting during the standard sample preparation. The subsequent calculation of the concentration in the initial sample for the experiment shown in Figure 5.5 generated 41 μg L^{-1} Hg^{2+}, while the expected concentration was 100 μg L^{-1} Hg^{2+}. A lower initial concentration than intended could of course be caused by inexact pipetting or miscalculation during the preparation of the experiment, but due to the unreasonable results from the calibration, the latter is more likely to be the reason. Therefore, the data shown in Figure 5.5 is based on the trend given by the ICP-MS analysis, but corrected to an initial concentration of 100 μg L^{-1} Hg^{2+}.

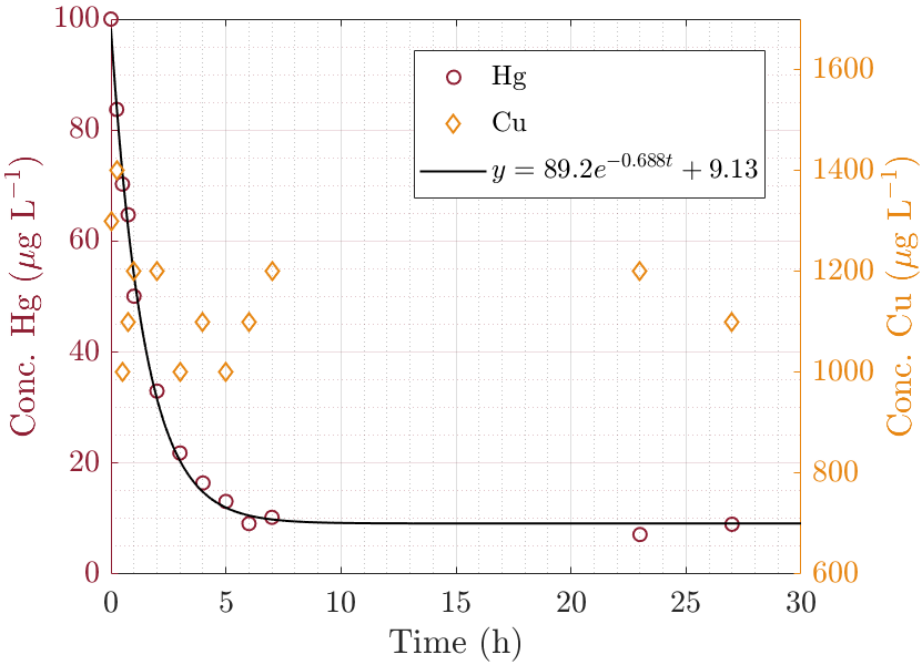

Figure 5.5: Hg^{2+} removal from tap water using a Cu sheet WE. An exponential fit to the data is also shown, as well as the amount of Cu in the water during the experiment.

Another possibly significant source of error in this experiment was the amount of Hg remaining in the instrument between washes. After running the standard series, the instrument is washed twice before running the samples from the experiment. However, during the second

wash for this particular analysis, a considerable amount of Hg was still left in the instrument. In fact, this amount of Hg was larger than the amount of Hg in all samples taken from 6 hours and forward. This has not been corrected for, due to the difficulties associated with quantifying the effect that this has had on the measurement. Nonetheless, this is likely the reason that the final concentration measured is around 9 μg L^{-1} Hg^{2+}. It is reasonable to believe that significantly less Hg^{2+} was left in the solution at the end of the experiment, and that the concentration converges towards zero.

The concentrations of Hg and Cu from the ICP-MS analysis of the Hg^{2+} removal experiment with the Cu foam electrode are shown in Figure 5.6. We can observe that the amount of Hg decreases rapidly over time, while the concentration of Cu remains approximately constant, similar to the Cu sheet experiment. Needless to say, sources of error are always present when performing experiments, however the specific problems related to the ICP-MS analysis described for the Cu sheet experiment are expected to be of much less significance in this experiment. These samples were analysed separately from those in Figure 5.5; the calibration generated reasonable results and the amount of Hg between washes was negligible. When comparing the experiments in Figure 5.5 and 5.6, it is important to note that the time-scales of the experiments are different, and that the Hg^{2+} ions are removed much faster from solution by the Cu foam WE than the Cu sheet WE.

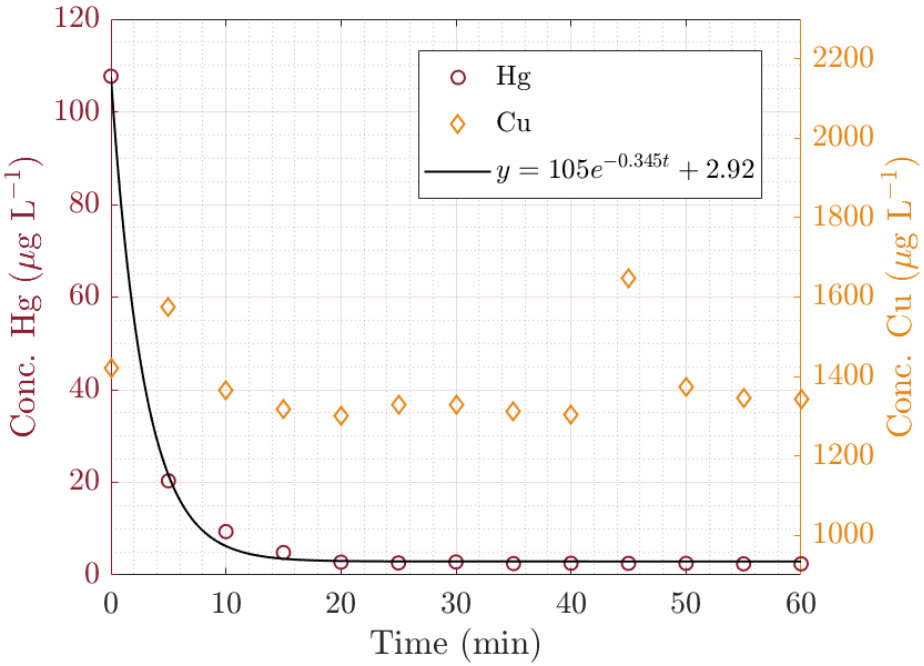

Figure 5.6: Hg^{2+} removal from tap water using a Cu foam WE. An exponential fit to the data is also shown, as well as the amount of Cu in the water during the experiment.

5.2.1.3 Comparison between Hg^{2+} removal rates and ECSA for Cu electrodes

Exponential functions on the form $y = C_0e^{-kt} + D$ are fitted to the Hg data in Figure 5.5 and 5.6, for comparison of the removal rate of the two experiments. The coefficients k in these expressions provide a measure of the rate of Hg^{2+} removal for a certain electrode. However, to obtain a meaningful value for comparison with the ESCA determined in Section 5.2.1.1,

we must also normalise with respect to the geometric surface area. The ratio between the coefficients is

$$\frac{k_{\text{foam}} A_{\text{sheet}}}{k_{\text{sheet}} A_{\text{foam}}} = \frac{0.345 \text{ min}^{-1} \cdot 5.8 \text{ cm}^2}{0.0115 \text{ min}^{-1} \cdot 3.4 \text{ cm}^2} \approx 51 \tag{5.4}$$

This value agrees remarkably well with the ratio of ECSA of the electrodes, 49. It must however be noted that the measurement of the ECSA primarily can be considered an order of magnitude estimate, and that the faradaic contributions to the current are expected to introduce an error in the area determination. In addition, the rate of Hg^{2+} removal for the Cu sheet contains a degree of uncertainty, due to the issues related to the ICP-MS analysis. The excellent agreement between these experiments is therefore somewhat surprising; it is however possible that the different sources of error cancel out in this case. Despite the experimental uncertainties discussed here, we can conclude this section by remarking that the Hg^{2+} removal rate of the Cu electrodes studied in this project seems to scale rather well with the ECSA.

5.2.2 Pt electrodes

Despite the high cost of Pt, its stability during almost all conceivable conditions, especially in a wide pH range, makes it the most feasible material for most industrial applications, some of which are studied in detail in Chapter 6. Designing an efficient reactor for such applications requires knowledge of how the reaction rate scales with ECSA and how the surface structure of the electrode affects this. Therefore, we now proceed with a study of the relation between Hg^{2+} removal rate and ECSA for Pt electrodes.

5.2.2.1 Determination of ECSA of Pt electrodes

The ECSA of Pt electrodes was measured as described in Section 4.3.1. A CV in the range $0-1.4$ V at a scan rate of 50 mV s^{-1} is shown in Figure 5.7 for the Pt thin-film electrode. The main features of a typical Pt CV are indicated in the figure. The method for determination of the ECSA of a Pt surface presented in Section 3.1.7 is based on measuring the current corresponding to H^+ adsorption. Thus, the current is integrated in the range indicated by the shaded area in Figure 5.7. The total charge Q is then obtained by division with the scan rate, to translate the integration variable from potential to time, upon which the ECSA can be calculated using equation (3.11):

$$\text{ECSA} = \frac{695 \ \mu\text{C}}{0.77 \cdot 210 \ \mu\text{C cm}^{-2}} = 4.30 \text{ cm}^2 \tag{5.5}$$

As the geometric area A of this specific Pt thin-film electrode was 1.49 cm^2, the RF of the electrode can be determined by equation (3.10):

$$\text{RF} = \frac{4.30 \text{ cm}^2}{1.49 \text{cm}^2} = 2.9 \tag{5.6}$$

This is a typical value of the RF for a poly-crystalline Pt surface, and can be assumed to be the same for all Pt thin-film electrodes, as they are fabricated by an identical process.

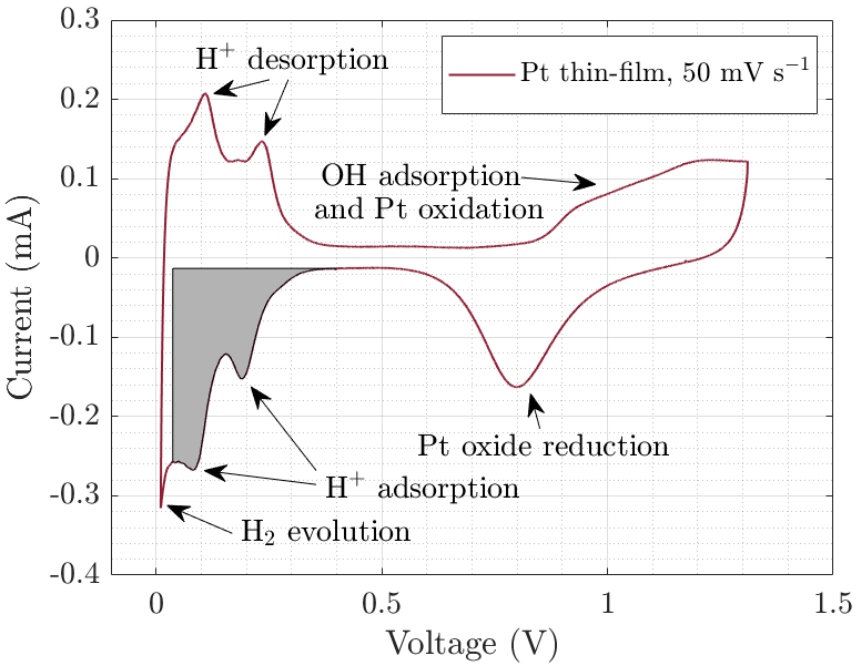

Figure 5.7: CV for a Pt thin-film electrode, from 0 to 1.4 V, with a scan rate of 50 mV s^{-1}. The main features of the CV are indicated in the figure. The shaded area corresponds to the integrated current associated with H^+ adsorption.

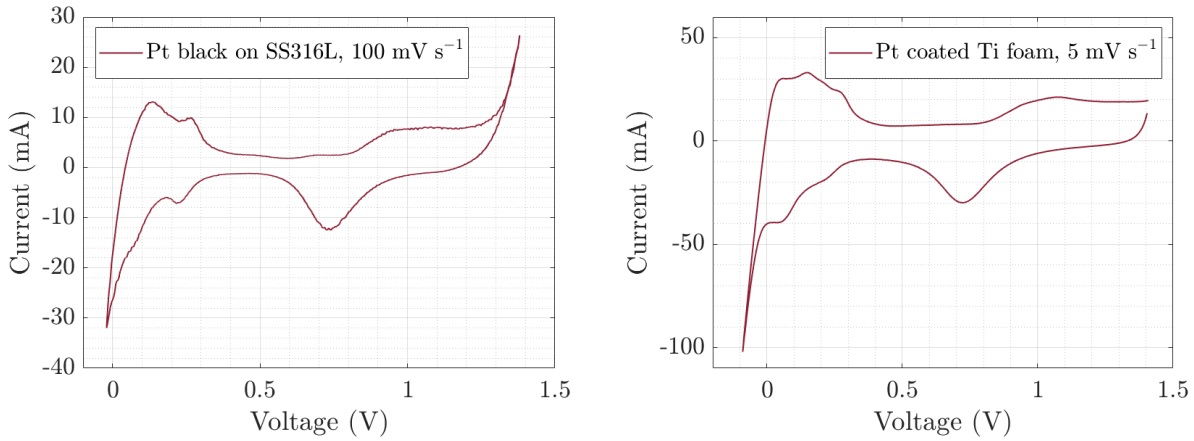

Figure 5.8: CV curves for a Pt black electrode (left) and the Pt coated Ti foam B electrode (right). The scan rate for the Pt black electrode was 100 mV s^{-1} and for the Ti foam 5 mV s^{-1}.

In Figure 5.8, the CV curves for a Pt black electrode and a Pt coated Ti foam electrode are shown. The typical features of a Pt CV are visible also in these plots, though, in addition, the Pt black electrode CV also shows a steel oxidation peak above 1.3 V. Both CV curves in Figure 5.8 extend to potentials slightly below 0 V, and thus, the H_2 evolution peak is much more pronounced compared to the Pt thin-film electrode CV. It can also be observed that especially the H^+ adsorption and desorption current peaks are less noticeable for the CV curves in Figure 5.8 than for the Pt thin-film electrode. The reason for this is likely that the Pt surfaces on the Pt black and Ti foam electrodes are not ideal poly-crystalline surfaces, as the PVD fabricated Pt thin-film electrode is. It might also be related to resistance effects

due to the large surface area of these electrodes. The CV shown in Figure 5.8 corresponds to Ti foam B, however the CV curves for Ti foams A and C are practically identical. The ECSA of the Pt black and the Ti foam electrodes are determined by the same procedure as for the Pt thin-film electrode, and the results are summarised in Table 5.1. Instead of a RF for the Pt coated Ti foam electrodes, a normalised foam area in cm^2 of ECSA per cm^3 of foam is given, as this is considered a more relevant quantity for a foam. The tabulated value of the surface area of a metal foam with average pore size 1.4 mm is approximately 25 cm^2 cm^{-3}, i.e. more than one order of magnitude lower than the ECSA measured here.

Table 5.1: Geometric areas, volumes, ECSA, RF and foam areas for the Pt electrodes.

Electrode	Geometric area	Volume	ECSA	RF	Normalised foam area
Pt thin-film	1.49 cm^2	N/A	4.30 cm^2	2.9	N/A
Pt black	4.2 cm^2	N/A	125 cm^2	30	N/A
Ti foam A	N/A	8.25 cm^3	4 480 cm^2	N/A	540 cm^2 cm^{-3}
Ti foam B	N/A	8.16 cm^3	5 680 cm^2	N/A	700 cm^2 cm^{-3}
Ti foam C	N/A	8.64 cm^3	8 000 cm^2	N/A	890 cm^2 cm^{-3}

5.2.2.2 Hg^{2+} removal from 0.5 M H_2SO_4 using Pt electrodes and comparison with the ECSA

This section presents the results from Hg^{2+} removal experiments with Pt electrodes, as described in Section 4.4.2. Figure 5.9 shows the ICP-MS analysis results from the Hg^{2+} removal experiments with Pt thin-film and Pt black WE. Exponential fits (the solid lines) to the data are also shown. The dashed and dashed-dotted lines represent theoretical prediction of the experiments, based on the MATLAB model described in Section 5.1.2. Note that the MATLAB model is by no means a fit to the experimental data, but instead produces the expected concentration curve given the same input parameters (electrode area, temperature, initial concentration) as for the experiment. We can begin to note that the MATLAB model fits very well to the initial data for the Pt thin-film electrode. The prediction always converges towards 0, while in reality usually some amount of Hg remains in the solution, which is the reason for the deviation between the experimental data and the prediction during the latter part of the experiment. Another contributing factor may be insufficient washing during the ICP-MS analysis. However, the MATLAB model is able to accurately reproduce the initial behaviour of experiments.

Moving on to the results for the Pt black electrode; it has a RF which is 10 times larger than the RF of a Pt thin-film electrode, and thus an equivalent area of 42 cm^2. The grey dashed-dotted line in Figure 5.9 shows the results from the MATLAB model with 42 cm^2 as the area input parameter. According to this prediction, the Hg^{2+} removal was expected to be much faster compared to what the experimental data shows. Therefore, another prediction was made using the MATLAB model, with simply the geometric area of 4.2 cm^2 as the input parameter, which is shown by the grey dashed line in Figure 5.9. This appears to be a better fit to the experimental data, which indicates that the equivalent area useful for Hg^{2+} removal might be much smaller than the ECSA for the Pt black electrode.

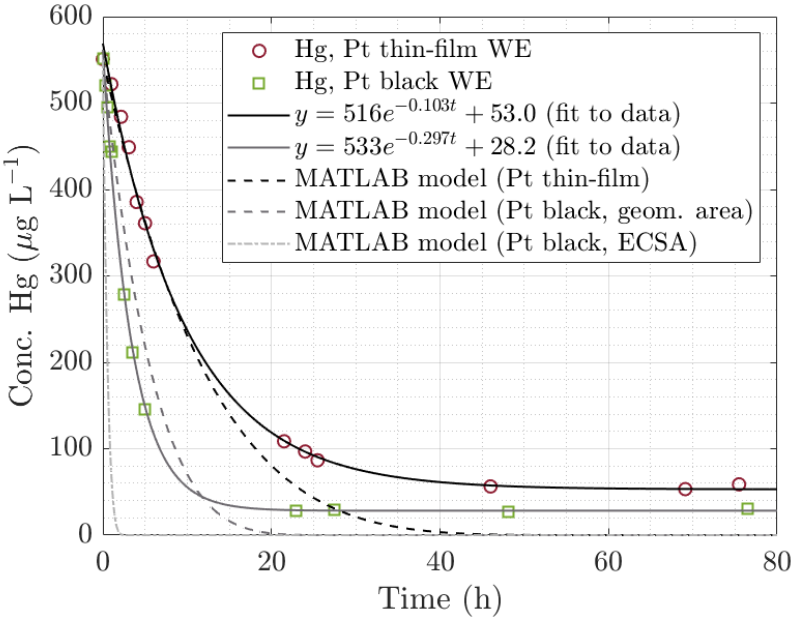

Figure 5.9: Hg^{2+} removal from 0.5 M H_2SO_4 using a Pt thin-film WE and a Pt black WE. Exponential fits to each data set are also shown, as well as theoretical predictions based on a MATLAB model.

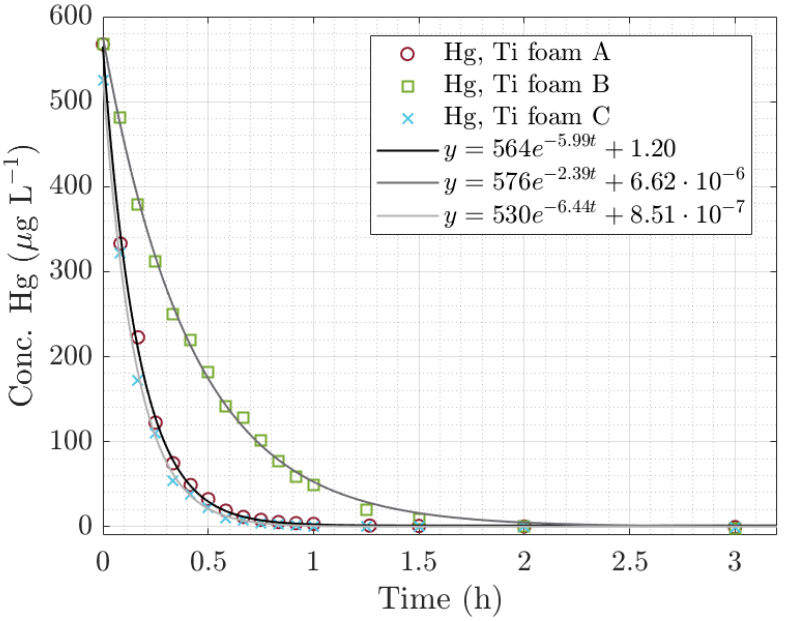

Figure 5.10: Hg^{2+} removal from 0.5 M H_2SO_4 using Pt coated Ti foams. Exponential fits to each set of data are also shown.

A similar analysis as for the Cu electrodes in Section 5.2.1.3 gives the ratio between Hg^{2+} removal rates for the two Pt electrodes, normalised to their geometric surface area:

$$\frac{k_{\text{black}} A_{\text{thin-film}}}{k_{\text{thin-film}} A_{\text{black}}} = \frac{0.297\ \text{h}^{-1} \cdot 1.99\ \text{cm}^2}{0.103\ \text{h}^{-1} \cdot 4.2\ \text{cm}^2} \approx 1.37 \tag{5.7}$$

Thus, even though the Hg^{2+} removal appears to be slightly faster for the Pt black electrode in Figure 5.9, this is almost entirely explained by the larger geometric surface area of the Pt black electrode. Evidently, the tenfold increase in RF (and ECSA) can not be translated into an increased rate of Hg^{2+} removal, as was possible for the Cu sheet and Cu foam electrodes.

We now proceed with the Hg^{2+} removal experiments using Pt coated Ti foam electrodes. The ICP-MS analysis results for these experiments are shown in Figure 5.10, together with exponential fits to the data. One might notice that the data for Ti foams A and C are practically identical, while the Hg^{2+} removal appears to be slower for Ti foam B. The reason is probably poor electrical contact during experiment B, or some other experimental issues, as the potentiostat experienced problems with overload during the experiment, and both the WE and CE had obtained a black surface coating afterwards. Thus, the different etching times for the three foams do not appear to affect the Hg^{2+} removal properties.

The rate of Hg^{2+} removal can now be compared with the ECSA for the Ti foams. In this comparison, the Pt thin-film electrodes will serve as a reference. For Ti foam A, normalised to 1 cm^3 of the foam, we obtain

$$\frac{k_{\text{foam A}} A_{\text{thin-film}}}{k_{\text{thin-film}} A_{\text{foam A}}} = \frac{5.99\ \text{h}^{-1} \cdot 1.99\ \text{cm}^2}{0.103\ \text{h}^{-1} \cdot 8.25\ \text{cm}^3} \approx 14 \tag{5.8}$$

Thus, the Hg^{2+} removal rate for 1 cm^3 of the Ti foam is 14 times faster than for 1 cm^2 of the Pt thin-film electrode. However, the ECSA of Ti foam A is 540 cm^2 per cm^3 of the foam, or 125 times larger than 1 cm^2 of the Pt thin-film electrode, and hence, it appears as most of the ECSA of the foam can also not be translated into an increased rate of Hg^{2+} removal, similarly as for the Pt black electrodes.

5.2.2.3 Pt black characterisation by SEM imaging

In order to understand the large deviation between the ECSA and Hg^{2+} removal rate for Pt black electrodes, SEM characterisation of these electrodes was performed. SEM images of a Pt black electrode are shown in Figure 5.11 at magnifications 5, 10, 50 and 100k. We can begin to note that the Pt black layer does not cover the entire surface, so that there are regions of steel exposed. At the lower magnifications, a structure which appears to be made up by 1 μm sized Pt spheres is visible. The spheres themselves are however built up by flakes with a typical size of 100 nm, which are visible at the higher magnifications. Both of these structures give rise to the large ECSA measured, as, ideally, each Pt atom exposed on the surface should adsorb one H^+.

5.2.2.4 Relation between ECSA and Hg^{2+} removal rates

To summarise the findings of this section, we can note that the Hg^{2+} removal rates measured for both the Pt black and the Ti foam electrodes are much lower than expected, considering their large ECSA. For the Pt black electrodes, there are two possible explanations for the relatively low Hg^{2+} removal rates observed, based on the SEM images of the electrode surface structure. Either the size difference between H^+ and Hg^{2+} comes into play, in that the Hg^{2+} ions can not reach into many of the smallest voids accessible to H^+ ions, or, perhaps more

likely, as soon as the Pt−Hg alloy formation starts, the surface structure of the Pt black layer changes so that the smallest voids are filled and the ECSA decreases rapidly.

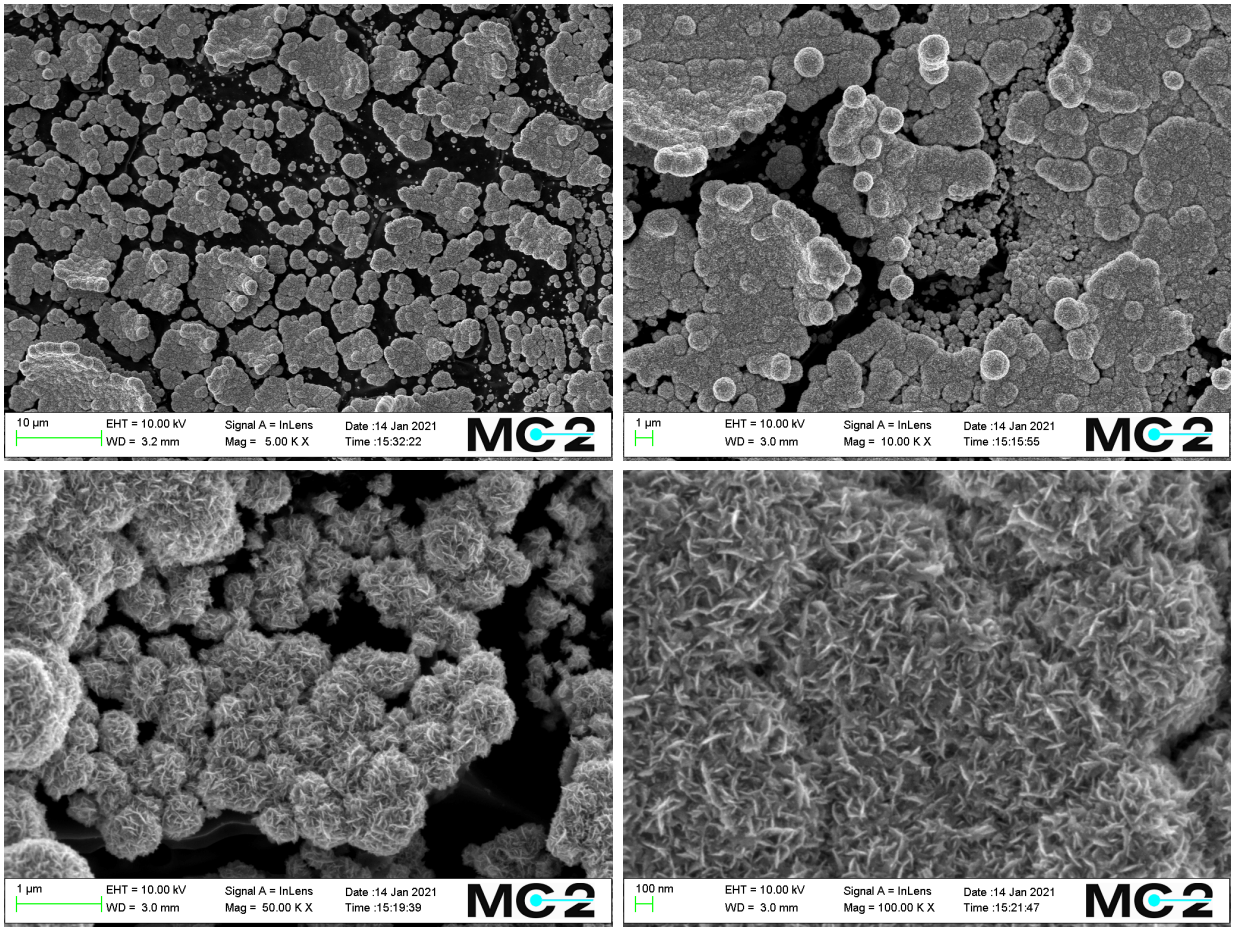

Figure 5.11: SEM images of Pt black on a SS316L substrate, at magnifications 5, 10, 50 and 100k.

As the Ti foam electrodes were not characterised using SEM, their surface structure is unknown. A reasonable guess is however that the structure resembles the Pt black structure, in that the ratio of ECSA is 10−20 times larger than the ratio of Hg^{2+} removal rates, compared to a Pt thin-film electrode. However, the Hg^{2+} removal rate, which is 14 times faster than on a Pt thin-film electrode, is in better agreement with the tabulated foam surface area of 25 cm^2 cm^{-3} [46] than with the ECSA. These values do however not correspond perfectly to each other, and there are a few possible explanations for the deviation. First, the tabulated value is based only on the average pore size of an arbitrary metal foam, and the exact relation between pore size and surface area may differ between different foams. In addition, as the Ti foams have not been studied using SEM, there is no certainty that the Pt coating covers the entire foam surface. There may be substantial amounts of Ti exposed, and those areas will not contribute to Hg^{2+} removal.

6
Case studies

In this chapter, two different case studies are presented, where the prospects of applying electrochemical alloy formation for Hg decontamination in industrial settings are evaluated. In Section 6.1, Hg removal from scrubber liquids from a combined heat and power plant is investigated. Section 6.2 addresses the issue with Hg contamination of concentrated H_2SO_4 produced by Boliden. In this study, electrode materials and suitable potentials are evaluated, followed by a pilot test where the Hg removal process is up-scaled 400 times.

6.1 Case study: Hg removal from scrubber liquids

Heat and electricity can be produced by incineration of waste in a combined heat and power plant. However, in this process, several different waste products are produced, e.g. Hg containing acidic scrubber liquids. The pH of the scrubber liquids typically lies in the range -1−0, and the flow rate is $2-4$ m^3 h^{-1}, 24 hours a day, all year round. The amount of Hg in the scrubber liquids can vary, and the temperature of the liquids in the process is typically around 50 °C. In this section, we will investigate the possibility of using electrochemical alloy formation to treat the scrubber liquids. Two different samples of scrubber liquids were provided from a combined heat and power plant in Denmark.

6.1.1 Hg removal from scrubber liquids using Ti fibre electrodes

The experimental details will first be described briefly in this section, before moving on to the results. The two scrubber liquids provided will from now on be denoted A and B. A thermostated glass vessel, connected to a water bath (Julabo F12-ED), was used to set the temperature to 50 °C, in order to get as close as possible to the conditions in the industrial process. Each experiment was performed using 50 mL of the scrubber liquid. A three electrode system was used, with a Ag/AgCl RE, a Pt wire as CE and a Ti fibre WE (described in Section 4.1.1.3), and the potential was set to 0.18 V.

The results from the ICP-MS analysis of the samples taken during the experiments are shown in Figure 6.2. The initial concentration of Hg in scrubber liquid A was 3 800 μg L^{-1}, and in scrubber liquid B 400 μg L^{-1}. As the initial concentrations differ with one order of magnitude, the Hg concentrations are shown in % of the initial amount in Figure 6.2. The trend of Hg removal is similar in both scrubber liquids, however the Hg concentration in scrubber liquid B seemingly saturates around 20%. Most likely, this does not reflect the actual Hg removal during the experiment, but is rather an effect of poor washing during the ICP-MS analysis (see Section 5.2.1.2 for more details). As much as 75% of the measured Hg content in the last samples from scrubber liquid B might originate from Hg remaining

in the ICP-MS system after washing.

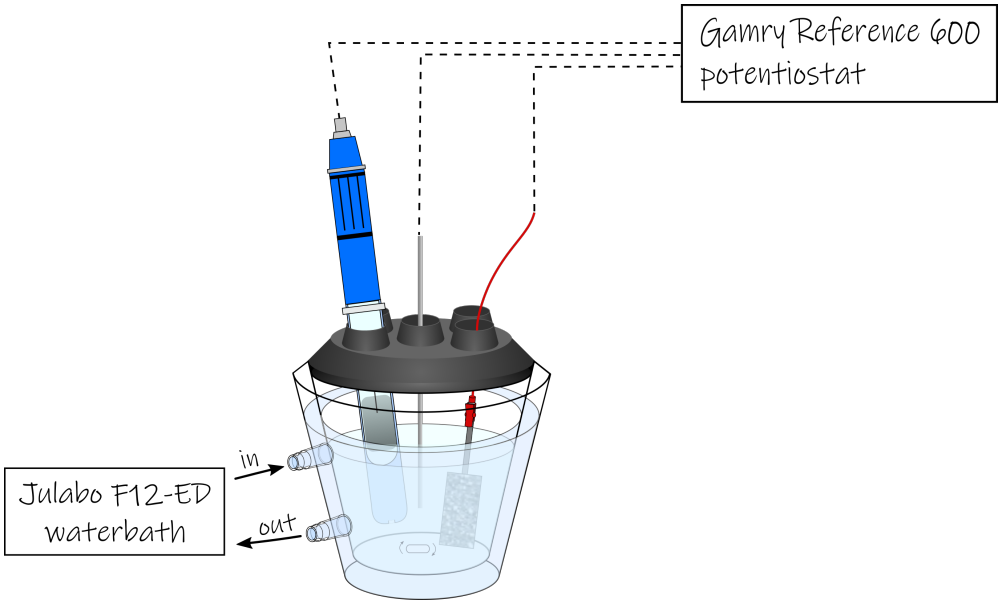

Figure 6.1: The experimental setup for removal of Hg from 50 mL scrubber liquid. The setup consists of a three electrode system with a Ti fibre electrode as the WE, a Ag/AgCl RE and a Pt wire as CE. A Gamry Reference 600 potentiostat was used to apply 0.18 V to the WE, and a Julabo F12-ED water bath to set the temperature to 50 °C.

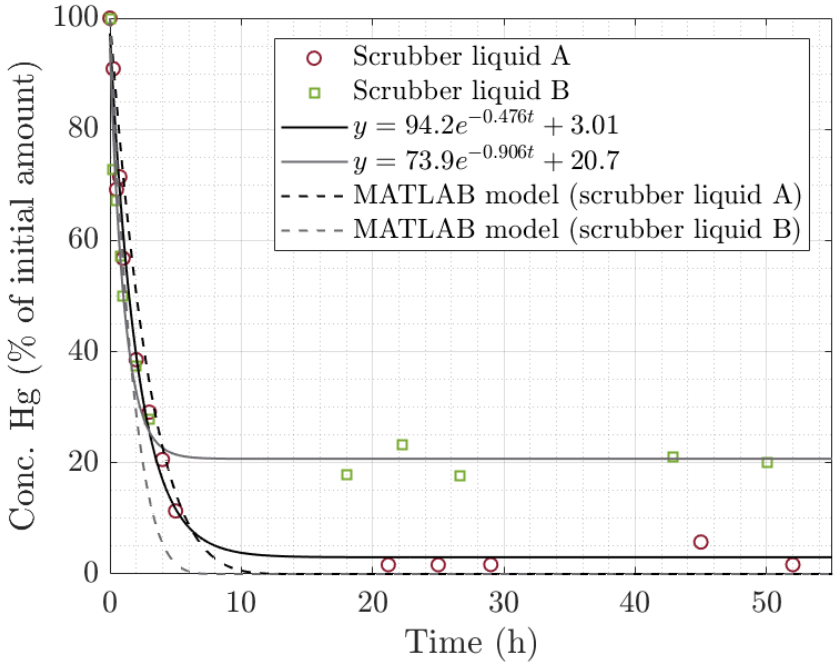

Figure 6.2: ICP-MS analysis results of the scrubber liquids from the Hg removal experiments. Exponential fits to each set of data points are also shown, as well as theoretical predictions based on a MATLAB model.

6.1.2 MATLAB model comparisons

Theoretical predictions, using the MATLAB model described in Section 5.1.2, of the Hg removal from the scrubber liquids are also shown in Figure 6.2. Input parameters given to the model were the geometric surface area of the Ti fibre electrodes, the temperature 50 °C, and the initial concentrations measured by the ICP-MS. We can observe that the trends of the theoretical predictions agree very well with the experimental data, which is somewhat surprising as the Ti fibre electrodes are expected to provide an increased surface area and, thus, and increased rate of Hg removal, compared to Pt thin-film electrodes which are the basis for the MATLAB model. The implication from this is that either the Ti fibre substrate does not provide an increased surface area accessible for Hg removal, or the Hg removal rate is affected by the fact that the composition of the scrubber liquids differ from the standard lab electrolyte of 0.5 M H_2SO_4.

6.2 Case study: Hg removal from concentrated H_2SO_4

Every year, 1.7 million tonnes of H_2SO_4 is produced by Boliden. In 2020, the Kokkola smelting plant in Finland alone had a production of over 300 kilotonnes. The H_2SO_4 contains various amounts of Hg, and is classified according to the Hg concentration. The acid can be classified as *technical quality* if it contains less than 300 μg kg^{-1} Hg, and as *bleaching quality* if it contains less than 80 μg kg^{-1} Hg.[1] Depending on the quality of the acid, it can be used in different industries and applications. However, the Hg content in the H_2SO_4 produced might occasionally exceed the acceptable amount for technical quality, which can limit the usefulness of the acid. Therefore, it would be desirable to have a method for removal of Hg from the H_2SO_4, to improve its quality.

In this project, which is a collaboration between Chalmers, Boliden and the start up company Atium, Hg removal from H_2SO_4 from the Kokkola plant is investigated. One of the challenges with concentrated H_2SO_4 is finding an electrode material that has a high stability and is compatible with the acid. Initially, different electrode materials were evaluated in the usual batch size of 50 mL. Considering the large annual production of H_2SO_4 at the Kokkola plant, the Hg removal process must however be up-scaled to treat much larger volumes. Therefore, this project also includes the up-scaling of the process to a 20 L pilot reactor. The goal was to reach below the 300 μg kg^{-1} required for the acid to be classified as technical quality in less than one week of electrochemical treatment.

6.2.1 Initial material evaluations for WE and CE for removal of Hg from concentrated H_2SO_4

The main challenge for removal of Hg from concentrated H_2SO_4 is finding suitable electrode materials for both WE and CE, which remain stable in the acid and, in the case of a WE, is able to successfully remove Hg by electrochemical alloy formation. Cu is not stable in concentrated H_2SO_4, and hence the choice of active material for the WE was Pt. For the removal to be as efficient as possible, a large surface area electrode, e.g. a foam or fibrous

[1] Note that Boliden measures all concentrations in μg kg $^{-1}$, and therefore, the concentrations in this section will also be given in μg kg^{-1}, as opposed to the rest of this thesis, where concentrations are given in μg L^{-1}.

material is desirable. However, due to the fact that Pt is a scarce resource that comes at a very high cost, a substrate material is needed to provide the large surface area. After examining materials such as Ti, and various kinds of steels, the stainless steel 316L was chosen as the substrate for this project. SS316L is an alloy consisting of Fe, Cr, Ni, Mo, C, Mn, P, S, Si and N [47]. Both 316 and 316L are austenitic steels, known for their corrosion resistance, where the 316L has a lower C content than 316.

Two initial tests were performed to evaluate the stability and performance of the materials, using SS316L sheets sputtered with Pt (described in Section 4.1.1.3). In both experiments, a three electrode system was used, the batch size was 50 mL, and the potential was set to 0.18 V. The RE was a Ag/AgCl electrode. In Exp. 1, the CE was a Pt wire, however in Exp. 2, a 40 mm x 40 mm diamond electrode (DIACHEM, Condias) was used as CE. The diamond electrode provides a larger surface area, which is expected to be important when moving towards larger surface area WE, and is known to be corrosion resistant. The experimental details of these, and the following experiments of this section, are summarised in Table 6.1.

Table 6.1: Experimental details of all Hg removal experiments performed using the concentrated H_2SO_4 from the Kokkola plant.

Experiment	Batch size	WE	CE	Potential/current
Exp. 1	50 mL	SS316L sheet with Pt	Pt wire	0.18 V
Exp. 2	50 mL	SS316L sheet with Pt	Diamond	0.18 V
Exp. 3	50 mL	SS316L foam with Pt	Diamond	0.08 V
Exp. 4	20 L	SS316L foam with Pt	Diamond	-2.98 V between WE and CE
Exp. 5	20 L	SS316L foam with Pt	Diamond	-0.7 A

The ICP-MS analysis results from Exp. 1 and 2 are shown in Figure 6.3. We can observe that Hg is removed from the acid in both experiments, however the removal is rather slow. Technical quality is reached for Exp. 1 after around 50 hours. The difference in initial concentration of the two experiments is unexpected, given that both were performed using acid from the same bottle, provided from the Kokkola plant. The reason for this difference is still unknown, but might be caused by a deviation in the standard solutions prepared for the ICP-MS analysis. Regardless of the difference in absolute values, we can conclude that the Hg concentration follows the same trend in both experiments. The concentration of Pt increases rapidly in the beginning of the experiments, which indicates that the Pt film on the WE is not completely stable in the concentrated H_2SO_4. Following the initial increase in concentration, the Pt content of the acid decreased slowly over time in Exp. 2, while the Pt content in Exp. 1 showed large variations, with a slightly increasing trend.[2] Regardless of this increase of Pt in the acid, the WE were deemed stable, as no visible degradation was observed, and the acid remained clear throughout the experiment. The difference in Pt content in the two experiments might be related to the stability of the Pt wire used as CE in Exp. 1. As the choice of CE did not affect the Hg removal efficiency, the diamond CE was chosen for the following experiments in this project, given its larger surface area and possibly better stability. Increasing the rate of Hg removal from the acid was the second

[2]Quantification of the amount of Pt in the acid was not possible for these experiments, as no Pt standards were prepared for the ICP-MS analysis.

issue to be addressed, and this is treated in the following sections.

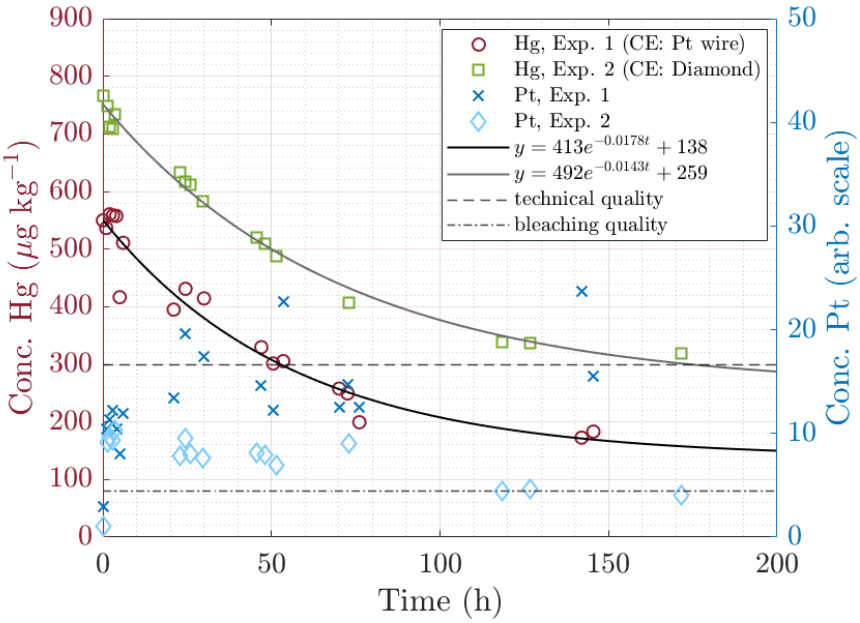

Figure 6.3: Hg removal from concentrated H_2SO_4 using a SS316L WE with 200 nm Pt. Two different experiments are shown; in Exp. 1 a Pt wire was used as CE, and in Exp. 2 a 40 mm x 40 mm diamond electrode was used as CE. An exponential fit to each data set is also shown, as well as the Pt concentration during the experiment.

6.2.2 Investigation of electrochemical reactions present in concentrated H_2SO_4

The potential in Exp. 1 and 2 was chosen to be 0.18 V, as the Pt−Hg alloy was known to form at that potential in 0.5 M H_2SO_4. Applying an even lower potential might increase the driving force for the alloy formation reaction, however it is also desirable to stay at a potential well above H_2 evolution. As H_2 evolution includes H^+ ions, the potential of this reaction, and the SHE potential scale, is pH dependent, as discussed in Section 3.1.3. Therefore, it might be possible to apply a lower potential to the WE in the concentrated H_2SO_4. A LSV experiment was performed in order to investigate which reactions take place in concentrated H_2SO_4 at the relevant potentials, and to determine the potential of H_2 evolution. A three electrode system was used, with a Ag/AgCl RE, a diamond CE and a Pt thin-film WE. The linear sweep began at 1.01 V (open circuit potential) and the potential was then decreased with a scan rate of 1 mV s^{-1}. Two potential sweeps were performed, one where the electrolyte was bubbled with Ar gas, and one without bubbling, in order to get information about the reactions in the presence and absence of O_2. The potential sweep was ended when H_2 evolution was clearly visible, around -0.3 V.

The $I - V$ curves for the LSV experiments are shown in Figure 6.4. For the sweep without Ar gas, the current first begins to drop around 0.3 V, before flattening out on a plateau at -2.7 mA, between 0.12 and 0.03 V. After 0.03 V, the current again begins to drop, and gas evolution at the WE becomes visible. Thus, it could be concluded that the current drop beginning at 0.03 V corresponds to H_2 evolution. If we now turn our attention to the

LSV with Ar bubbling of the electrolyte, only one current drop is visible, and the plateau has disappeared. Thus, we can conclude that the first current drop of the linear sweep without Ar corresponds to O_2 reduction. The amount of O_2 in the electrolyte decreases when bubbling with Ar, which moves the O_2 reduction towards lower potentials. The total current of the O_2 reduction current peak is also expected to decrease, moving the plateau towards higher currents, however the two current peaks merge together in the Ar bubbling case, so that the plateau disappears. Nonetheless, the conclusion could be drawn that 0.18 V provides a larger than necessary safety margin to H_2 evolution, and, thus, the following experiment was decided to run at 0.08 V.

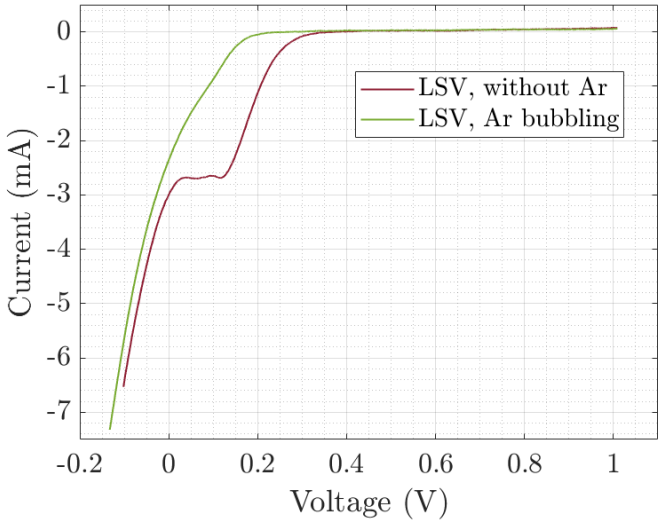

Figure 6.4: $I-V$ plot for the LSV experiments, with and without Ar bubbling of the electrolyte.

6.2.3 Increasing the Hg removal rate from concentrated H_2SO_4

To increase the rate of Hg removal compared to the experiments shown in Figure 6.3, a larger surface area WE was necessary. The SS316L foam described in Section 4.1.3 was therefore chosen as the WE for the following experiments. The stability of the SS316L foam was verified by immersing it in concentrated H_2SO_4 for 7 days. No visible degradation of the foam or colour change of the acid occurred during these 7 days. The same test was performed after the foam had been platinised, in which case a slight colour change of the acid in the vicinity of the foam could be observed after 4 days. Thus, it was evident that the foam was less stable after the platinisation procedure, which was not entirely unexpected as the Pt plating was performed in a high temperature molten salt solution. One possible explanation for the decreased stability of the foam might be a change in surface composition of the stainless steel alloy, caused by the high temperature plating process.

One experiment, Exp. 3, was performed using the SS316L foam as a WE. The setup was otherwise identical to that of Exp. 2 and is shown in Figure 6.5. The potential was set to 0.08 V, as decided based on the LSV experiment. However, as indicated by the WE degradation test, the stability of the foam had decreased after the platinisation process, and about 5 hours into the experiment, the electrolyte was visibly discoloured and cloudy. After 48 hours, the acid began to clear up, and the magnetic stirrer had received a grey coating,

indicating that at least some part of the discolouring might originate from Fe, which then attached to the magnet. Another conclusion is that the stability of the WE is potential dependent, as the discolouring of the acid appeared much faster with 0.08 V applied than without any potential.

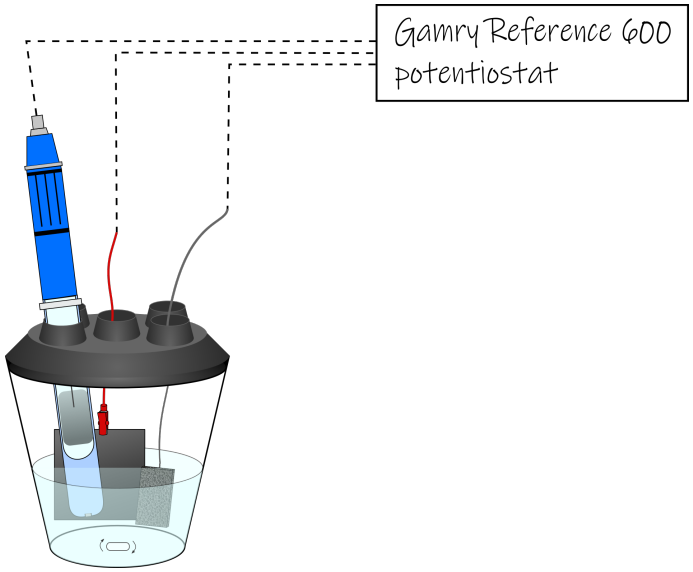

Figure 6.5: The experimental setup for removal of Hg from 50 mL concentrated H_2SO_4 from the Kokkola plant. The setup consists of a three electrode system with a Pt coated SS316L foam as the WE, a Ag/AgCl RE and a diamond electrode as CE. A Gamry Reference 600 potentiostat was used to apply 0.08 V to the WE.

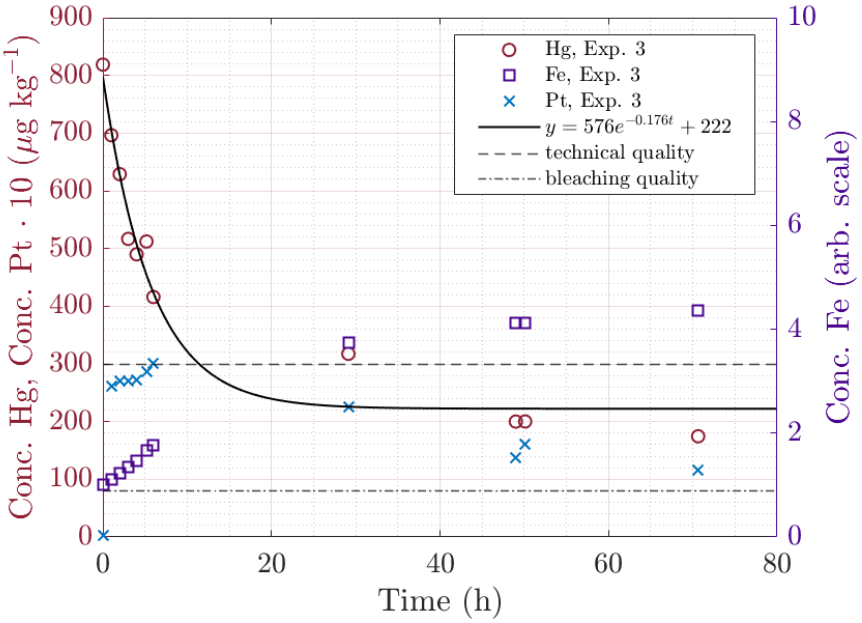

Figure 6.6: Hg removal from concentrated H_2SO_4 using SS316L foam coated with Pt. An exponential fit to the data is also shown. The amounts of Fe and Pt in solution during the experiments are also shown.

The ICP-MS analysis results of Exp. 3 are shown in Figure 6.6. The decrease in Hg concentration was fast compared to Exp. 1 and 2, and technical quality was reached after about 12 hours according to the exponential fit. It is however notable that the exponential function does not fit very well to the experimental data. As expected, we can also note that the concentration of Fe increased to about 4 times the initial concentration throughout the experiment. The Pt content of the acid increased rapidly in the beginning of the experiment, similar to Exp. 1 and 2, however after the initial increase, the amount of Pt again began to decrease. This resembles the behaviour of Cu in a weakly acidic environment, where Cu is initially released to the electrolyte, and then re-adsorbs during the experiment [5].

6.2.4 Pilot test – Hg removal from 20 L concentrated H_2SO_4

This section presents the pilot study attempting to scale up the Hg removal process in the case of concentrated H_2SO_4. The aim was to treat 20 L of H_2SO_4 in one week and reach technical quality.

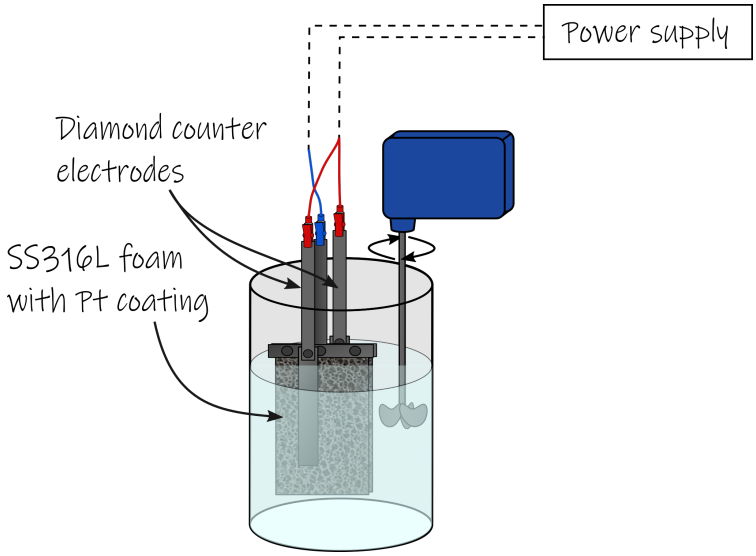

Figure 6.7: The experimental setup used in Exp. 4 and 5 for removal of Hg from 20 L concentrated H_2SO_4 from the Kokkola plant. The setup consists of a two electrode system with a Pt coated SS316L foam as the WE, two diamond electrodes as CE. A power supply is used to apply a constant potential or current between the WE and CE.

The up-scaled experiments were performed in a setup built by Atium. The setup is shown in Figure 6.7 and consisted of a 30 L SS316L reactor, two 200 mm x 20 mm x 6 mm diamond coated Si CE (DIACHEM, Condias), two 210 mm x 270 mm x 3 mm Pt coated SS316L foams, of the same type as in Exp. 3, as WE and a stirrer. The electrolyte was 20 L of concentrated H_2SO_4 from the Kokkola smelting plant. Two different experiments were performed using this setup. As the use of a RE is unfeasible at this scale, the experiments were conducted in a two electrode setup. A Ag/AgCl RE was used during the setup of Exp. 4 in order to obtain the same potential between WE and CE as in Exp. 3. However, the uncertainty in the determination of this potential in the two electrode setup was rather large, as the measured potential between WE and RE was dependent on the placement of the RE in the reactor. Therefore, the potential was adjusted during the initial part of the experiment, so that -2.78 V was applied between WE and CE between $0 - 1$ hour, -3.18 V

between $1 - 2.5$ hours and -2.98 V from 2.5 hours forward. Due to the uncertainty in the determination of a suitable potential, during Exp. 5 the power supply was instead used to apply a constant current to the WE. The current was determined by scaling up the current measured after 20 hours in Exp. 3 to obtain the same current density. A current of -0.7 A was therefore applied during Exp. 5.

The results from the ICP-MS analysis of Exp. 4 are shown in Figure 6.8. In general, all features of Exp. 3 in the 50 mL batch are repeated in the 20 L batch. The electrolyte was discoloured and cloudy during both experiments, similar to the 50 mL batch experiment. Technical quality is reached after less than 20 hours, and the concentration of Hg is very close to the bleaching quality limit at the end of the experiment, after 75 hours. To investigate whether bleaching quality would have been reached, had the experiment just been given more time, Exp. 5 was run for 165 hours. The results from Exp. 5 are shown in Figure 6.9, and we can observe that bleaching quality is indeed reached around 70 hours. As both Exp. 4 and 5 were performed in a lab without heating, the temperature during the experiments was also monitored, and the temperature fluctuations during the experiments are presented in Figures 6.8 and 6.9.

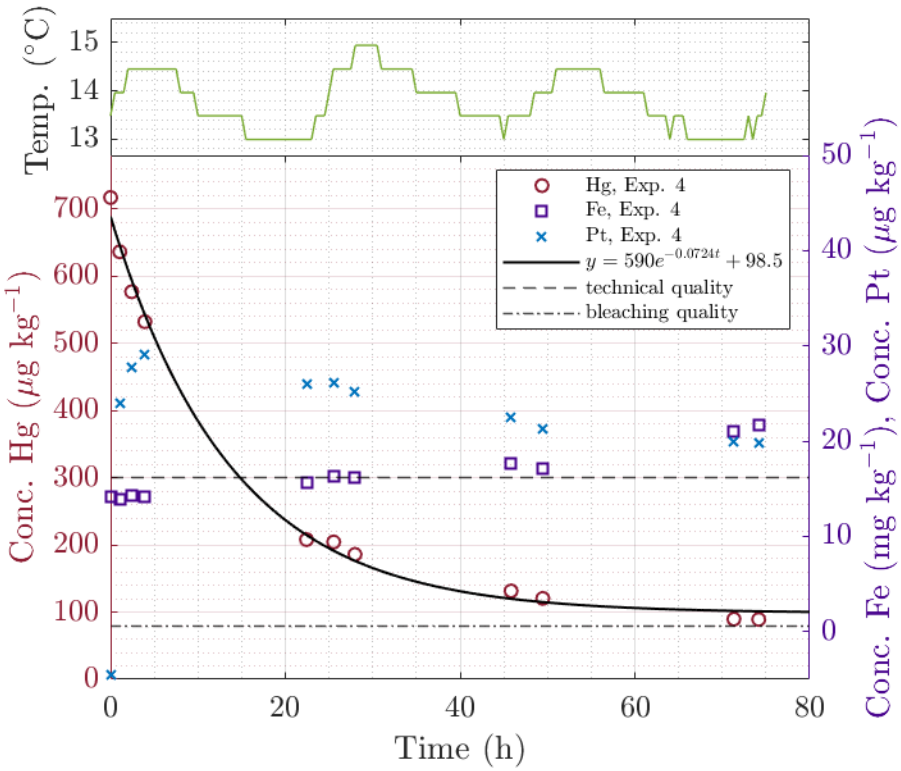

Figure 6.8: Hg removal from 20 L concentrated H_2SO_4 from the Kokkola plant. An exponential function is fitted to the data, and the concentration limits for technical and bleaching quality are indicated in the figure. The concentrations of Fe and Pt in the acid during the experiments are also shown, as well as the temperature during the experiment.

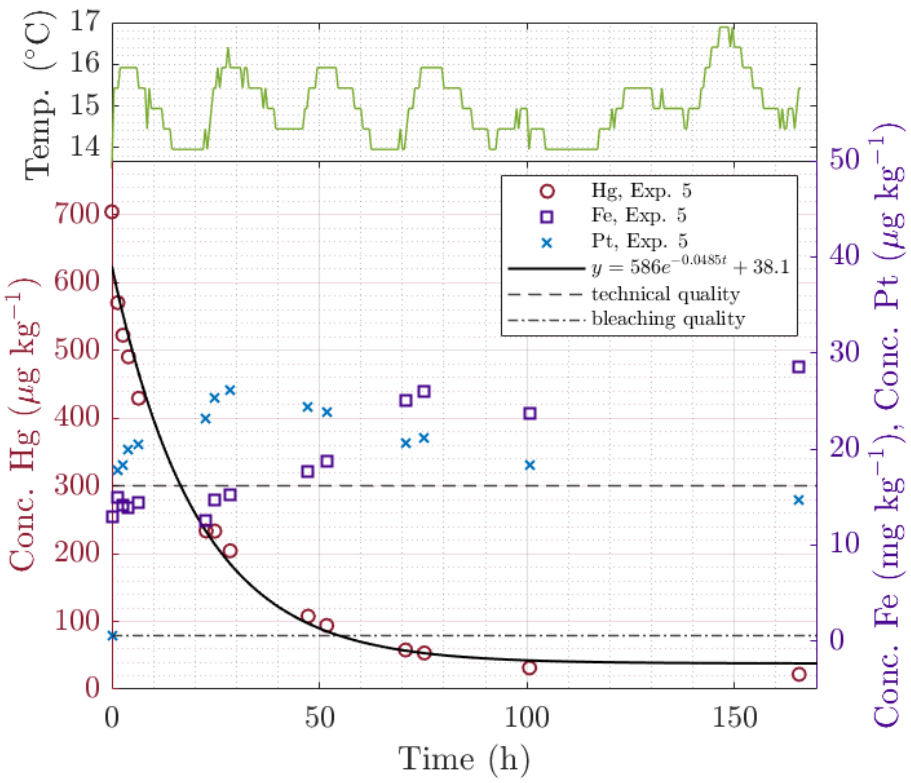

Figure 6.9: Hg removal from 20 L concentrated H_2SO_4 from the Kokkola plant. An exponential function is fitted to the data, and the concentration limits for technical and bleaching quality are indicated in the figure. The concentrations of Fe and Pt in the acid during the experiments are also shown, as well as the temperature during the experiment.

A comparison between Exp. 3, 4 and 5 is shown in Figure 6.10. The initial decrease in Hg concentration is very similar for all three experiments, however the 50 mL batch experiment (Exp. 3) does not reach as low final concentrations as the 20 L batch experiments. A summary of all experiments with the concentrated H_2SO_4 from the Kokkola plant is given in Table 6.2, where the times for 20, 50 and 80% Hg removal are calculated based on the fitted exponential functions. When comparing these values, it is important to be aware of the poor fit of the exponential function to the data from Exp. 3, which seemingly result in the calculated times in Table 6.2 underestimating the actual times for Hg removal. In addition to this, the 20 L batch experiments were performed at lower temperature than the 50 mL batch experiments, which according to the activation energy measured in this thesis, corresponds to a reaction rate that is 20−30% lower. Further, the ratio between electrode surface area and electrolyte volume was approximately 40% higher in the 20 L experiments than in Exp. 3. Hence, these effects will virtually cancel each other out. The conclusion that can be drawn from these experiments is that up-scaling of the Hg removal process is possible, without any significant loss of efficiency.

Table 6.2: Times of 20, 50 and 80% Hg removal, for all experiments with the concentrated H_2SO_4 from the Kokkola plant, according to the exponential fits.

Hg removal	Exp. 1	Exp. 2	Exp. 3	Exp. 4	Exp. 5
20%	17 h	25 h	1.8 h	3.7 h	4.9 h
50%	62 h	100 h	6.7 h	12 h	16 h
80%	N/A	N/A	N/A	38 h	39 h

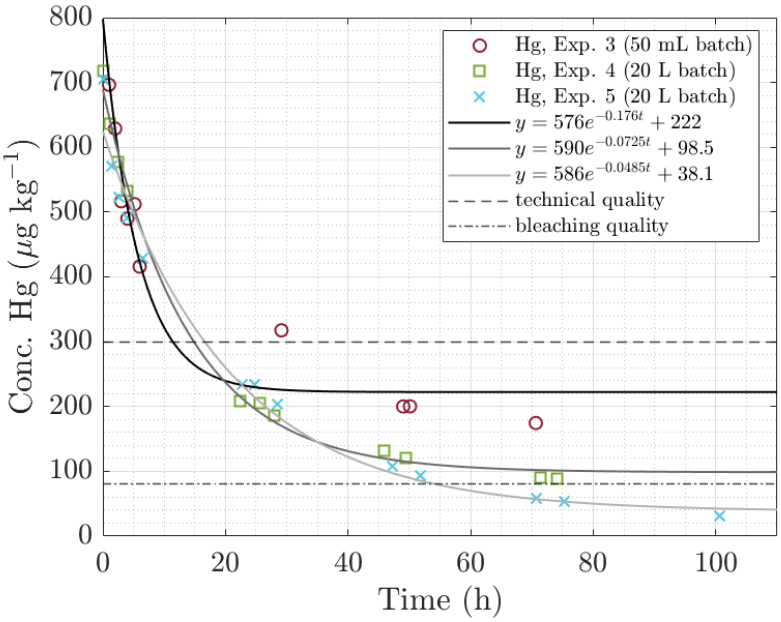

Figure 6.10: Hg removal from concentrated H_2SO_4 using SS316L foam coated with Pt. Three different experiments are shown; Exp. 3 (50 mL) and Exp. 4 and 5 (20 L). Exponential fits to each set of data are also shown, as well as the technical and bleaching quality limits.

7

Conclusion and outlook

This chapter will summarise the main results and conclusions from each part of the project, as well as present suggestions for future studies on electrochemical alloy formation.

7.1 Temperature dependence and activation energy of the Pt−Hg alloy formation

The activation energy of the Pt−Hg alloy formation was determined to 0.29 eV, and this result was incorporated in a MATLAB model which has proved to give accurate predictions of mercury removal under various conditions. This model will be of great value in the continued research, however, additional research into the reaction mechanism of the alloy formation could further improve and refine the model. There are still many unanswered questions about the Pt−Hg alloy formation reaction mechanism, and more detailed and sophisticated studies, for example studying the energy dissipation signal from the electrochemical quartz crystal microbalance could lead to new insights.

7.2 Relation between electrode surface area, surface structure and mercury removal efficiency

We have shown that for both the Pt−Hg and the Cu−Hg systems, the rate of alloy formation can be enhanced by increasing the surface area of the electrode. However, the alloy formation rate only increases with surface area for large structures, such as a metal foam, with typical pore sizes around 0.5−1.5 mm. A large surface area originating from a porosity on the nanometer length-scale, as for a platinum black layer, does not contribute to an increased rate of mercury removal. This thesis does however not answer the question about the optimal feature size (e.g. optimal foam pore size) for maximum mercury removal efficiency per unit volume, so that would be an interesting area for the continued research. As the surface structure has proved to be of importance, combining mercury removal experiments with more scanning electron microscopy characterisation, also for the metal foam surfaces will be vital in the continued research.

7.3 Mercury removal from industrial wastewaters

The technology has proved to efficiently remove mercury from acidic scrubber liquids from a combined heat and power plant. The next step for this specific application would be to further increase the reaction rate, perhaps by using a titanium foam electrode rather than

the fibrous titanium substrate used in this thesis. Scrubber liquids is however only one example of industrial waste products in need of mercury decontamination, and common for practically all of the potential applications is the need of decontamination of flowing water. Thus, the most important next step towards real applications of this technology is undoubtedly to build an understanding of how the alloy formation works in flowing water. Here, both experiments and a theoretical model could be of value, to understand how the mercury removal efficiency depends on the flow rate, in order to be able to optimise the design of the reactor and corresponding electrode materials.

7.4 Mercury removal from concentrated sulphuric acid

We have also shown that mercury can efficiently be removed from concentrated sulphuric acid by electrochemical alloy formation. Thus, the most important focus of further research in this area is to improve the stability of the electrode materials. Finally, the up-scaling of the process in the specific case of concentrated sulphuric acid without any loss of efficiency is a very important result. The implication from this is that experiments can be performed at lab scale, e.g. to evaluate materials and mercury removal efficiencies, and that the results will be valid also at an industrial scale.

7.5 General suggestions for future research

The potential dependence of the alloy formation has been briefly discussed in this thesis, however not thoroughly investigated. A more detailed study of the potential dependence is of interest both in order to improve on the understanding of the alloy formation reaction, but also to optimise the potential for applications. Regeneration of platinum electrodes is another important area for continued studies of the Pt−Hg system, which has not been addressed in this thesis. Studying the mechanisms of the regeneration process, and especially how the electrode structure is affected by regeneration will be of importance here.

Bibliography

[1] Pure Earth/Blacksmith. *The World's Worst Pollution Problems 2012: Assessing Health Risks at Hazardous Waste Sites*. Tech. rep. 2012.

[2] Pure Earth/Blacksmith. *2016 World's worst pollution problems*. Tech. rep. Pure Earth, Green Cross Switzerland, 2016.

[3] Noelle E. Selin. "Global Biogeochemical Cycling of Mercury: A Review". In: *Annual Review of Environment and Resources* 34 (2009). DOI: 10.1146/annurev.environ.051308.084314.

[4] Cristian Tunsu and Björn Wickman. "Effective removal of mercury from aqueous streams via electrochemical alloy formation on platinum". In: *Nature Communications* 9.1 (2018). ISSN: 2041-1723. DOI: 10.1038/s41467-018-07300-z.

[5] Mattias K.O. Bengtsson, Cristian Tunsu, and Björn Wickman. "Decontamination of Mercury-Containing Aqueous Streams by Electrochemical Alloy Formation on Copper". In: *Industrial and Engineering Chemistry Research* 58.21 (2019), pp. 9166–9172. ISSN: 15205045. DOI: 10.1021/acs.iecr.9b01513.

[6] UN Environment. *Global Mercury Assessment 2013: Sources, Emissions, Releases, and Environmental Transport*. Tech. rep. 2013, p. 42.

[7] Jung Duck Park and Wei Zheng. "Human exposure and health effects of inorganic and elemental mercury". In: *Journal of Preventive Medicine and Public Health* 45.6 (2012), pp. 344–352. ISSN: 19758375. DOI: 10.3961/jpmph.2012.45.6.344.

[8] United Nations Environment. *Global Mercury assessment 2018*. Tech. rep. 2018, p. 270.

[9] WHO. *Mercury and health*. 2017. URL: https://www.who.int/en/news-room/fact-sheets/detail/mercury-and-health.

[10] WHO. *Exposure to Mercury: A major public health concern*. Tech. rep. 2007, p. 4. DOI: 10.1016/j.ecoenv.2011.12.007.

[11] UN Environment. *Mercury general information*. URL: https://www.unenvironment.org/explore-topics/chemicals-waste/what-we-do/mercury/mercury-general-information.

[12] WHO. *Guidelines for Drinking-water Quality*. Tech. rep. 2017.

[13] The European Parliament and the Council of the European Union. *Directive (EU) 2020/2184 of the european parliament and of the council of 16 December 2020 on the quality of water intended for human consumption*. Tech. rep. December. 2020, pp. 1–62.

[14] Grégorio Crini and Eric Lichtfouse. "Advantages and disadvantages of techniques used for wastewater treatment". In: *Environmental Chemistry Letters* 17.1 (2019), pp. 145–155. ISSN: 16103661. DOI: 10.1007/s10311-018-0785-9. URL: https://doi.org/10.1007/s10311-018-0785-9.

[15] Fenglian Fu and Qi Wang. “Removal of heavy metal ions from wastewaters: a review”. In: *Journal of environmental management* 92 (2011). ISSN: 1095-8630. DOI: 10.1016/j.jenvman.2010.11.011.

[16] Abhi Sharma and Anmol Sharma. “Removal of Mercury(II) from Aqueous Solution: A Review of Recent Work”. In: *Separation Science and Technology (Philadelphia)* 50 (2015). ISSN: 15205754. DOI: 10.1080/01496395.2014.968261.

[17] J Patterson. “Capsule Report: Aqueous Mercury Treatment”. In: *U. S. Environmental Protection Agency* July (1997).

[18] Sarabjeet Singh Ahluwalia and Dinesh Goyal. “Microbial and plant derived biomass for removal of heavy metals from wastewater”. In: *Bioresource Technology* 98.12 (2007), pp. 2243–2257. ISSN: 09608524. DOI: 10.1016/j.biortech.2005.12.006.

[19] D. A. Atwood and M. K. Zaman. “Mercury removal from water”. In: *Structure and Bonding*. Vol. 120. November 2005. 2006, pp. 163–182. ISBN: 3540312544. DOI: 10.1007/430{_}013.

[20] Jin Gang Yu and Bao Yu Yue. “Removal of mercury by adsorption: a review”. In: *Environmental Science and Pollution Research* 23.6 (2016), pp. 5056–5076. ISSN: 16147499. DOI: 10.1007/s11356-015-5880-x.

[21] Mojtaba Taseidifar et al. “Removal of heavy metal ions from water using ion flotation”. In: *Environmental Technology and Innovation* 8 (2017), pp. 182–190. ISSN: 23521864. DOI: 10.1016/j.eti.2017.07.002. URL: http://dx.doi.org/10.1016/j.eti.2017.07.002.

[22] Virapan, R Saravanane, and V Murugaiyan. “Treatment of Reverse Osmosis Reject Water from Industries”. In: *International Journal of Applied Environmental Sciences* 12.3 (2017), pp. 489–503. URL: http://www.ripublication.com.

[23] A. Dabrowski and Z. Hubicki. “Selective removal of the heavy metal ions from waters and industrial wastewaters by ion-exchange method”. In: *Chemosphere* 56 (2004). ISSN: 00456535. DOI: 10.1016/j.chemosphere.2004.03.006.

[24] Malcolm Barlow and Peter John Planting. “Heterometallic Phenomena in the Platinum-Mercury System”. In: *Zeitschrift Für Metallkunde* 60 (1968), pp. 292–297.

[25] S. K. Lahiri and D. Gupta. “A kinetic study of platinum-mercury contact reaction”. In: *Journal of Applied Physics* 51.10 (1980), pp. 5555–5560. ISSN: 00218979. DOI: 10.1063/1.327440.

[26] M Z Hassan, D F Untereker, and Stanley Bruckenstein. “Ring-disk study of thin mercury films on platinum”. In: 42 (1973), pp. 161–181.

[27] Zenko Yoshida. “Structure of Mercury Layer Deposited on Platinum and Hydrogen-evolution Reaction at the Mercury-coated Platinum Electrode”. In: *Bulletin of the Chemical Society of Japan* 54.2 (1981), pp. 556–561. ISSN: 0009-2673. DOI: 10.1246/bcsj.54.556. URL: http://www.journal.csj.jp/doi/10.1246/bcsj.54.556.

[28] Emma Feldt. “Electrochemical removal of mercury from contaminated aqueous solutions”. 2019.

[29] Allen J. Bard and Larry R. Faulkner. *Electrochemical methods : fundamentals and applications*. Wiley, 2001. ISBN: 0471043729.

[30] Richard G. Compton and Craig E. Banks. *Understanding Voltammetry*. 3rd. Imperial College Press, 2018. ISBN: 9781786345295.

[31] D K Nordstrom and F D Wilde. “Reduction - Oxidation Potential (Electrode Method)”. In: *U.S. Geological Survey TWRI Book*. Vol. 9. January 1998. 1998. Chap. 6.5.

[32] S. Szabó and I. Bakos. "Reference electrodes in metal corrosion". In: *International Journal of Corrosion* 2010 (2010). ISSN: 16879325. DOI: 10.1155/2010/756950.

[33] "Electro-Analytical Chemistry".

[34] S. Trasatti and O. A. Petrii. "Real Surface Area Measurements in Electrochemistry". In: *Pure and Applied Chemistry* 63.5 (1991), pp. 711–734. ISSN: 13653075. DOI: 10.1351/pac199163050711.

[35] T. Biegler and D.A.J. Rand. "Limiting oxygen coverage on platinized platinum; Relevance to determination of real platinum area by hydrogen adsorption". In: *Journal of Electroanalytical Chemistry and Interfacial Electrochemistry* 29 (1971). ISSN: 0022-0728. DOI: 10.1016/S0022-0728(71)80089-X.

[36] Yuru Ge et al. "How to measure and report the capacity of electrochemical double layers, supercapacitors, and their electrode materials". In: *Journal of Solid State Electrochemistry* 24.11-12 (2020), pp. 3215–3230. ISSN: 14330768. DOI: 10.1007/s10008-020-04804-x.

[37] Daniel A. Buttry and Michael D. Ward. "Measurement of Interfacial Processes at Electrode Surfaces with the Electrochemical Quartz Crystal Microbalance". In: *Chemical Reviews* (1992). ISSN: 15206890. DOI: 10.1021/cr00014a006.

[38] Diethelm Johannsmann. *The Quartz Crystal Microbalance in Soft Matter Research*. Heidelberg: Springer, 2015. ISBN: 978-3-319-07835-9. DOI: 10.1007/978-3-319-07836-6.

[39] Donald M. Mattox. *Handbook of Physical Vapor Deposition (PVD) Processing*. 2nd. Elsevier, 2010. ISBN: 978-0-8155- 2037-5.

[40] Ashok K. Singh. "Experimental Methodologies for the Characterization of Nanoparticles". In: *Engineered Nanoparticles*. 2016. Chap. 4, pp. 125–170. ISBN: 9780128014066. DOI: 10.1016/b978-0-12-801406-6.00004-2.

[41] Christopher P. East et al. "Analytical Techniques to Characterize Scales and Deposits". In: *Mineral Scales and Deposits*. Ed. by Zahid Amjad and Konstantinos D. Demadis. Elsevier, 2015. Chap. 28. ISBN: 978-0-444-63228-9.

[42] Ludwig Reimer. *Scanning Electron Microscopy*. Ed. by Peter W. Hawkes. 1985, pp. 1–388. ISBN: 9783642282515. URL: http://download.springer.com/static/pdf/262/bok:978-3-642-28252-2.pdf?auth66=1391844428_9b049bc3bc66000ff127949721c341e8&ext=.pdf%5Cnpapers2://publication/uuid/C40BB93A-C9AE-4A08-A2EE-B3E2C534A0CE.

[43] Elsevier Sequoia S A et al. "Investigation of the compound formed at a platinum-mercury interface". In: 23 (1969), pp. 343–349.

[44] G. R. Souza and I. A. Pastre. "Solid state reactions in the platinum–mercury system". In: *Journal of Thermal Analysis and Calorimetry* 88 (2007). ISSN: 1388-6150. DOI: 10.1007/s10973-006-8037-9. URL: http://link.springer.com/10.1007/s10973-006-8037-9.

[45] Julia Järlebark et al. "Elektrokemisk legeringsbildning av PtHg4 i syfte att rena vatten från kvicksilver". 2019.

[46] Fraunhofer IFAM. *Open cell metal foams*. Tech. rep. 2016. URL: http://www.ifam.fraunhofer.de/content/dam/ifam/en/documents/dd/Infobl%C3%A4tter/open_cell_metal_foams_fraunhofer_ifam_dresden.pdf.

[47] Sandemeyer Steel Company. *Specification Sheet : Alloy 316 / 316L*. Tech. rep. 2014.